Observation and Parameterization of Solar Irradiance in Marine Stratocumulus and Cumulus Regimes

by
Sean C. Gillies and Stephen K. Cox

Department of Atmospheric Science
Colorado State University
Fort Collins, Colorado

Colorado State University

Department of Atmospheric Science

Paper No. 590

OBSERVATION AND PARAMETERIZATION OF SOLAR IRRADIANCE IN MARINE STRATOCUMULUS AND CUMULUS REGIMES

by: Sean C. Gillies and Stephen K. Cox

Department of Atmospheric Science
Colorado State University
Fort Collins, CO 80523

December 1995

Atmospheric Science Paper No. 590

ABSTRACT

OBSERVATION AND PARAMETERIZATION OF SOLAR IRRADIANCE IN MARINE STRATOCUMULUS AND CUMULUS REGIMES

As part of the ASTEX campaign in June of 1992, intensive observations were made of the surface solar irradiance on the island of Porto Santo. From these data, the net surface irradiance has been derived for the period of June 1-28, 1992 and reduced into visible and infrared and direct and diffuse components. By comparison of data collected under partially-clouded and overcast conditions, the enhancement of the surface solar irradiance due to the finite properties of marine boundary layer clouds has been determined.

A parameterization has been developed to account for the finite geometry and horizontal inhomogeneity of the marine boundary layer clouds. Accounting for the finite size and vertical extent of cloud is shown to increase the effective cloud amount relative to the horizontal cloud cover. Accounting for the horizontal inhomogeneity in cloud liquid water path is shown to lead to an effective optical thickness that is smaller than the average optical thickness of the cloud. This parameterization is validated by comparison to the observations, using observed cloud liquid water paths and cloud cover in a simplified radiative transfer model. The reduced optical thickness parameterization is shown to be an improvement over the conventional parameterization which use an anomalously low amount of clouds which are uncharacteristically thick.

ACKNOWLEDGEMENTS

Table of Contents

Chapter 1. Solar Radiation and Clouds

1.1 Surface Solar Irradiance

To understand the Earth's climate system in a thermodynamic sense one must have an understanding of its primary heat source: flux of solar radiation. Solar irradiance drives much of the energy exchange between the atmosphere and land or ocean surfaces and thereby influences the dynamics of the atmosphere. The connection between radiative fluxes and atmospheric circulations is present on all scales from the microscale (such as turbulence over heated ground) to the mesoscale (stratocumulus circulations and sea breezes) to synoptic and planetary scale (monsoons and poleward transport of heat by the general circulation). To realistically model such circulations one must be able to realistically prescribe the spatial and temporal patterns of radiative heating of the climate system. Early general circulation models (GCMS) used global patterns of radiative heating that were derived from climatologies and were independent of the resolved variables of the model. This is useful when one is aiming to reproduce climatological circulations but is insufficient for modeling a changing climate. The most advanced contemporary GCMs carry important radiative components of the climate system (water vapor, carbon dioxide, cloud condensation nuclei) as prognostic variables and can

diagnose the water mass of a finite grid volume, thereby providing the input for realistic

radiative transfer models. These GCMs which have physically-based rather than arbitrary

radiant energy systems are likely to produce more realistic solar irradiances and more

realistic surface energy exchanges, which will allow better simulations than their

predecessors.

Climate modelers are not the only users of this quantity. Surface solar irradiance

is needed to assess cloud and aerosol effects, to determine the biological productivity of

the land and ocean, and to survey solar energy resources.

1.2 Approaches to Representing Solar Irradiance

The flux of solar radiation across a small surface can be measured by pyranometer,

however most of the need is for regional scale solar irradiance. When there is inadequate

coverage of a region by pyranometers, one must use other means to estimate the regional

irradiance. The approaches to deriving solar irradiance may be separated into empirical

and physical approaches (Pinker and Laszlo, 1992).

The simplest empirical methods consider optical air mass (secant of the solar

zenith angle), cloud cover and cloud density (Haurwitz, 1945). By using a regional-scale

cloud cover and cloud density in the empirical relation, a regional-scale irradiance is

obtained. A well-known empirical approach involves a quantity called *percent possible

sunshine*, the ratio of full sunshine to the time in which sunshine is possible (Rosenberg,

et al, 1983). The percent possible sunshine is related empirically to cloud cover and time

of year. The empirical approaches are easy to implement since they incorporate relatively

abundant information such as cloud cover observation but suffer because they are site-

specific and must be tuned to a particular region. Empirical methods can be improved by longer and more intensive sampling on a larger scale. Satellites equipped with radiometers allow the correlation of satellite-measured radiances to surface irradiance. Despite the global coverage from space, these methods still suffer from the lack of observations of surface solar energy.

In a physical approach to estimating surface solar irradiance, the transfer of radiation is simulated in a way which incorporates all the important physical interactions such as; absorption, emission, and scattering. This approach is the one with the most promise and will continue to improve as knowledge of the absorptive and scattering properties of the atmosphere improve. For the foreseeable future, the solar radiation within physical radiative transfer schemes will be calculated by two stream or four stream methods. These one dimensional radiative transfer methods are applicable to horizontally homogeneous and infinite plane parallel layers of atmosphere. They are computationally inexpensive and capable of estimating fluxes to within the 10 W m^{-2} that a GCM requires (Pinker *et al*, 1992). The grid volumes of a GCM, being at least 100 km across and less than a kilometer in thickness are practically infinite but for the same reason it is unrealistic to assume that they are homogeneous, especially when cloud is present. For example, consider an atmospheric column within a GCM which possesses a unstable lapse rate and moisture convergence. Based on knowledge of cumulus convection, it is certain that the liquid water that the GCM diagnoses to be present in the grid volume is not in the form of horizontally homogeneous stratus cloud, but is manifested in convective cells. It is to be expected that the average fluxes of solar radiation for these cases, even given

3

the same mass of liquid water, are very different. The fluxes in the atmosphere are, for broken, optically thick cloud conditions, more sensitive to the fractional coverage of cloud than to the optical thickness of the clouds. Even the more stratiform types of cloud exhibit inhomogeneous structure due to embedded waves or cells and therefore interact differently with solar radiation than ideal homogeneous layers (Stephens, 1988; Cahalan *et al*, 1994).

The conventional parameterization of the transfer of radiation on subgrid scales has been the use of an effective cloud amount for homogeneous plane-parallel clouds (Welch and Wielicki, 1985). Although this method can be used to treat the fluxes from a partially clouded layer, it evades the issue of horizontal cloud inhomogeneity and may lead to loss of information about the direct and diffuse components of the flux. The ratio of direct to diffuse irradiance is a climatologically important variable significant to studies of surface energy budgets (Pinker and Laszlo, 1992) and surface entropy budgets (Kelly, 1994).

We may anticipate that GCMs, or regional surface radiation algorithms, may soon be able to diagnose higher order moments of the liquid water distribution on the subgrid scales or perhaps even solve prognostic equations for the variance of water within a grid volume. The goal of the present research is to develop a parameterization for solar radiative transfer that will account for many of the effects of inhomogeneous cloudiness, that is applicable to the two stream methods of GCMs, and which requires no new information from the model other than the variance of the liquid water within the grid volume. The parameterization will be built upon the basis of two stream solutions to the

4

radiative transfer equation, the independent pixel approximation (Cahalan, 1989) and a statistical model of subgrid scale cloudiness. It is developed for single cloud layers but might be extended to several layers of cloud in the manner described by Morcrette and Fouquart (1986).

1.3 Objectives

The physical approach to estimating surface solar irradiance can be improved by accounting for the horizontal inhomogeneity of clouds which are used in the one-dimensional radiative transfer schemes of surface radiation budget programs and general circulation models. The following chapters of this thesis concern the parameterizations for cloud inhomogeneity and the measurements against which they are compared.

In Chapter 2 the nature of cloudiness in the Stratus-Trade Wind Cumulus transition regime as observed during ASTEX/FIRE II will be reported and compared to a cloud climatology . The cloudiness directly above the field site was detected with a ceilometer, bolometer, and radar. Values of vertically integrated cloud water were deduced from microwave measurements.

The solar radiation budget of the ocean surface and the impact of cloudiness within the transition regime is discussed in Chapter 3. The finite properties of clouds are shown to have the effect of increasing net surface solar radiation.

The problem of radiative transfer through inhomogeneous media and broken fields of finite clouds in particular is described in Chapter 4. The independent pixel approximation and the use of one dimensional methods for three dimensional transfer problems are considered in detail and the resultant uncertainties are reported.

Chapter 5 concerns the statistical model of subgrid scale cloudiness and how an integral expression of the independent pixel approximation leads to a parameterization for an equivalent reduced optical thickness. The details of the numerical integration that yields the ensemble reflection and transmission are presented. The albedo bias (Stephens *et al*, 1991; Cahalan *et al*, 1994) and the corresponding transmission bias have been computed for many instances and are discussed.

In Chapter 6, the parameterization is validated through simulation of the average surface solar irradiance for the ASTEX/FIRE II intensive field observation (IFO) and the daily average surface solar irradiance for each day of the IFO. Daily average, within this research, will be defined as the sum of measurements within a day divided by 24 hours. All following references to daily averages are 24-hour averages, not averages over the shorter daylight period.

This research has implications for several other problems of atmospheric radiative transfer, particularly the cloud albedo and absorption anomalies and the retrieval of cloud properties from satellite radiance measurements. Just as inhomogeneous distribution of water in a cloud layer increases the layer's transmission of solar radiation, it will decrease the amount of radiation reflected and absorbed. Satellite retrievals are likely to deduce optical thicknesses closer to the effective reduced optical thickness than the true optical thickness of a cloudy pixel and this may lead to underestimates of cloud water and droplet number density or overestimates of the size of cloud droplets.

Chapter 2. Cloudiness

2.1 Structure of the Cloud-topped Marine Boundary Layer

2.1.1 Regimes of Cloudiness

A brief discussion of the larger scale is in order to begin to understand the role that clouds play in the energy budget of the maritime atmosphere and ocean. Figure 2.1 schematically depicts the general circulation and the cloudiness which occurs near the subtropics.
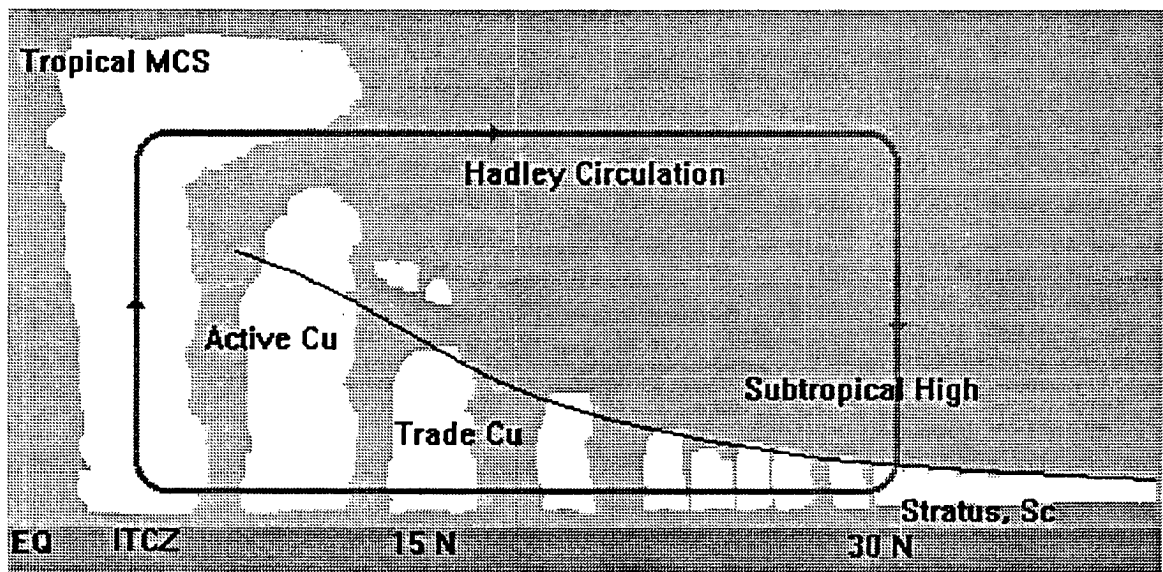

Figure 2.1. Structure of the trade wind-stratus transition.

7

Figure 2.1Figure 2.1 illustrates the situation in the Northern Hemisphere summer; the Intertropical Convergence Zone (ITCZ), the rising branch of the Hadley Circulation, is north of the equator and the subtropical ridge, the downward branch of the Hadley cell, is near 30 degrees north. Between these latitudes are the Trade Winds. The Hadley Circulation can be understood as an atmospheric heat engine which is driven by latent heating in the deep convective clusters of the ITCZ. The engine does work in the subtropics by pushing down upon the marine boundary layer. This constrains surface moisture fluxes in a shallow boundary layer and results in extensive and persistent sheets of cloud. Marine stratus cloud is an important factor of the Earth's radiation budget as it tends to have a large shortwave albedo and an infrared emmittance that is not much different than the underlying ocean. The net effect of marine stratus cloud, presumably, is to cool the ocean. The Atlantic Stratocumulus Transition Experiment (ASTEX) was carried out to study the processes which create and destroy the extensive sheets of cloud in the transition zone between the trade wind and subtropical stratus regimes.

2.1.2 Structure of the Trade Wind MBL

The trade-wind marine boundary layer (MBL) is composed of five distinct layers (Garstang and Betts, 1974): a shallow *surface layer*, a deeper *mixed layer* which is adiabatic and has a nearly homogeneous specific humidity, a *transition layer*, a conditionally unstable *cloud layer* which is inhabited by cumulus clouds, and an *inversion layer*. Trade-wind cumulus are of three types (Stull, 1985): *forced* clouds which mark the top of mixed layer thermals which reach the lifting condensation level but do not obtain the level of free convection (LFC), *active* clouds which do reach the LFC and become

positively buoyant and may even penetrate the stable inversion layer, and *passive* clouds which are decoupled from mixed layer thermals. Because the marine atmosphere is rather humid, passive cumulus may decay slowly and may account for a significant fraction of MBL cloud cover (Albrecht, 1981). Radiative forcing from these clouds may continue after they cease to interact dynamically with the MBL.

2.1.3 Structure of the Stratocumulus-topped MBL

The structure of the stratocumulus-topped MBL is much like that of the trade-wind MBL. Due to the stronger subsidence, the inversion is more pronounced and the depth of the entire MBL is shallower. The cloud layer may be coupled to the underlying mixed layer by strong surface fluxes or by strong radiative cooling in the cloud tops, or the cloud layer may be decoupled from the mixed layer when fluxes are small (Garratt, 1992). Cumulus have been observed to coexist with stratocumulus clouds and may serve to couple stratocumulus cloud to the mixed layer (Cotton and Anthes, 1989). Stratocumulus clouds during ASTEX exhibited droplet concentrations in the range of 30-500 cm^{-3} and effective radii from 6-12 μm. The larger droplets were associated with cumulus cells embedded with the stratocumulus decks and drizzle drops were also observed (Johnson, *et al*, 1992).

2.2 Climatology of Cloudiness in the FIRE II - ASTEX Region

2.2.1 Surface Observation

A comprehensive analysis of cloud cover by Warren *et al.* (1986) provides a ten year climatology of cloudiness over the ASTEX study region. Two weather stations in the Madeira Islands recorded over 13,000 observations of sky cover in the June, July, and

August months from 1971-1981. There is no unique relationship between the hemispheric sky coverage and the earth coverage of cloud. It is commonly assumed that reported sky coverage is always greater than the earth coverage due to the observation of cloud sides and the virtual concentration of cloudiness near the horizon. The ratio between the two is highly dependent on the vertical thickness and distance between clouds. In the case of shallow and extensive stratus and stratocumulus the difference between sky and earth coverage should be the smallest of all cloud types.

The mean cloud cover for the JJA season, the average of 13,000 observations, is 54 percent. The standard deviation of all, a measure of moment-to-moment variability, is 30 percent in absolute units (not 30 percent of the mean). The standard deviation of all JJA means, a measure of interannual variability, is 5 percent. Since this is calculated from only ten years of data, one must have little confidence in this value. The amplitude of the seasonal mean diurnal cycle of cloud cover is small, just 3 percent, and the mean time of maximum cloudiness is 1000 local time. At the Madeira Islands, this would be 1100 GMT. The simplest interpretation of the diurnal cycle in marine boundary layer (MBL) clouds is that they thicken at night due to condensation which balances a large radiative cooling rate and thin in the day when solar heating offsets the infrared cooling and stabilizes the sub cloud mixed layer (Garratt, 1992). The observed mid-morning peak in cloud cover is contrary to this simple conceptual model of MBL cloudiness and cannot be attributed to observer error, since overestimation of cloud cover is most likely at night. Further evidence of a mid-morning cloudiness maximum will be seen in ceilometer data from FIRE II/ASTEX.

The month of June, specifically, differs slightly from the entire summer season. Mean cloud cover for all days of June, 1971-1981, is 60 percent. For all June data, Warren *et al.* (1986) compiled the statistics which are shown in table 2.1. Cloud cover is the product of frequency of occurrence (FOC) and the amount when present (AWP). Also shown are the amplitude (in absolute percentage) of the diurnal cycle of cloud cover and the standard deviation of ten June means (1971-1981). Especially notable in the June observations is the extreme scarcity of cloudless days, which have a frequency of 2 percent, and the predominance of the stratus regime of cloudiness. The stratus, stratocumulus, and fog cloud also show the most variability on diurnal and interannual time scales.

Table 2.1 Cloud occurrence statistics for June data from 1971-1981

Cloud Type	FOC	AWP	Cover	Diurnal	Interannual
Cumulus	34	29	10	1.0	2.9
Cb	0	47	0	0.1	1.8
St, Sc, Fog	61	69	42	3.5	7.5
As, Ac	4	40	2	---	0.8
Cirrus	7	37	3	---	1.2
Clear	2	100	2	---	1.9

All values in table 2.1 are in units of percent sky cover, except for FOC. FOC is the frequency of occurrence, AWP is the amount when present, Cover is the sky coverage, Diurnal is the amplitude of the diurnal cycle, and Interannual refers to the standard

deviation of annual June means. The diurnal cycle is not reported in the clear class as it is undefined, and for high clouds because they are not reliably reported at night.

2.3 Cloudiness Observed During FIRE II - ASTEX IFO

2.3.1 Observation of Cloud Class

Rawinsondes were launched at three hour intervals, 203 in all, from the field experiment site on Porto Santo and some note was made of class and sky coverage of cloudiness at launch time. These observations of cloudiness are summarized in table 2.2.

Table 2.2 Observer identification of cloudiness

Cloud Class	Number
Stratus and Stratocumulus	62
Cumulus	36
Clear Sky	14
No Comment	91

The ratio of cumulus to stratus and stratocumulus observations are in general agreement with the climatology of Warren *et al.* (1986).

2.3.2 Ceilometer Measurement of Cloud Cover

A laser ceilometer was deployed at the field site to measure cloud base heights at two minute intervals. A detailed description of this instrument and its operation is found in Cox, et al., (1993). An hourly cloud cover fraction can be defined by the fraction of ceilings detected by the ceilometer within the hour. This cloud cover is earth coverage by cloud and is expected to deviate from hemispheric sky cover. The wavelength of the

12

ceilometer laser is 0.91 μm, therefore the cloud amount measured by the ceilometer is relevant to the transfer of near-infrared and, presumably, visible solar radiation. The ceilometer-derived cloud cover for the entire experiment is 48.5 percent. Hourly cloud cover throughout the experiment is shown in figure 2.2. An immediately notable quality of the ceilometer-derived cloud cover is intermittency. Hours of very clear or very overcast conditions are not random instances in this time series, but occur episodically. When cloud cover is analyzed for frequency of occurrence of cloud fraction (figure 2.3), it is observed that there are relatively large and equal instances of mostly clear (< 10 percent) and mostly cloudy (> 90 percent) conditions with a rather flat distribution of intermediate cloud cover. The mean diurnal variation in ceilometer-derived cloud cover can be seen in figure 2.4. Cloud cover is at a maximum of nearly 65 percent at about 0330 GMT and a minimum of 30 percent 12 hours later. The cloudiness minimum lags about 2.5 hours behind the Sun's closest approach to zenith (1300 GMT), indicating that solar heating is not the only determinant of cloudiness.

2.3.3 Infrared Radiometer Measurement of Cloud Cover

The PRT-6 infrared bolometer is another zenith-pointing instrument which can be used to estimate the frequency of cloud coverage. The PRT-6, its calibration, and manner of deployment at the field site are discussed in detail in Cox, et al, (1993a). 11 μm zenith radiance is measured by the PRT-6 and converted to an equivalent blackbody brightness temperature by inversion of Planck's Law. When the brightness temperature exceeds that typical of a cloudless atmosphere (roughly 220-230 K), cloud is present at zenith within the 2° field of view (FOV) of the PRT-6. A cloud cover fraction can be
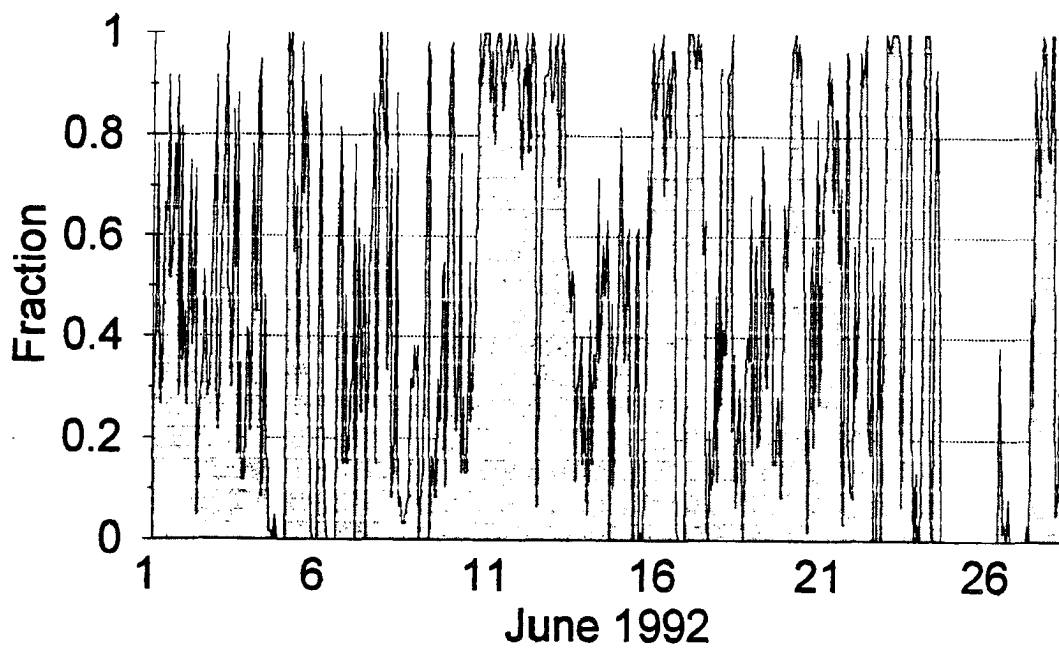
13

Figure 2.2. Hourly cloud cover determined from ceilometer
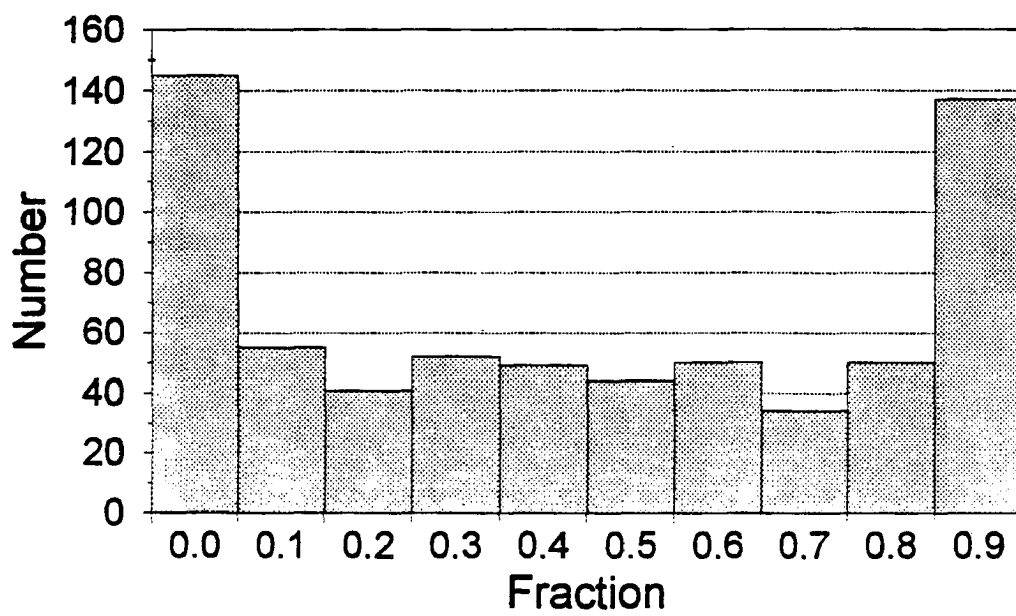
14

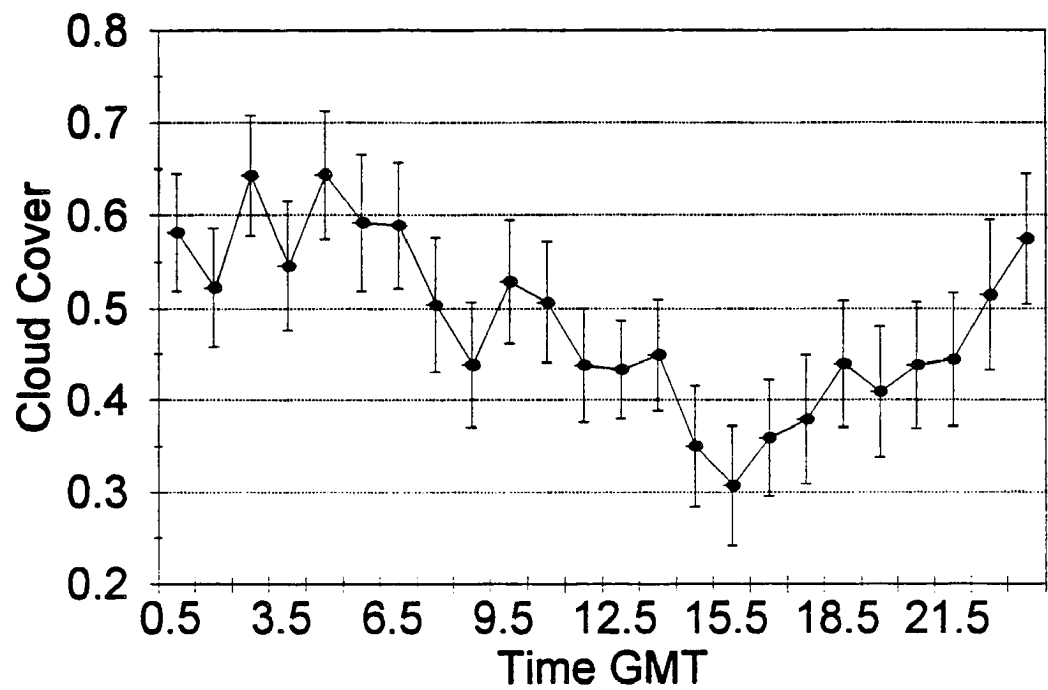Figure 2.3. Frequency of ceilometer cloud cover

Figure 2.4. Diurnal variation of ceilometer cloud cover. Error bars show one standard error.

derived from PRT-6 measurements by the same method as described in 2.3.1, where the cloud fraction is simply the number of brightness temperatures in an interval which exceed a threshold for cloudiness divided by the number of measurements made within the interval. A threshold of 240 K, based upon analysis of all PRT-6 data (Cox, *et al*, 1993b), has been used to derive hourly cloud cover data from the PRT-6 measurements. The average cloud cover measured by the infrared radiometer for the period of 2-28 June is 53 percent. Evidently, the PRT-6 is detecting the radiance from optically thin or elevated cloudiness that does not produce a significant return of the ceilometer pulse or is more sensitive to partially filled fields of view. This conclusion is also borne out by the histogram of cloud cover frequency shown in figure 2.5. The PRT-6 and ceilometer data indicate an almost equal frequency of nearly clear (< 10 percent) hours, 148 and 145 respectively. The PRT-6 detects much less intermediate cloudiness and many more nearly overcast (> 90 percent) hours, 217 to 137 as detected by the ceilometer. Figure 2.6 shows the mean diurnal variation in cloud cover as measured by PRT-6. The range is very near that which appears in the ceilometer data (30 to 70 percent). Another qualitative similarity between figures 2.4 and 2.6 is a mid-morning peak in cloudiness beginning near 1000 GMT, or about fours hours after solar heating begins. As previously mentioned, the mid-morning cloudiness peak also appears in the ten year climatology of Warren *et al.* (1986). It can also be seen in the fractional cloudiness estimates of Fairall *et al.* (1990) from FIRE at San Nicolas Island. This is an interesting phenomenon in light of suggestions that stratus breakup and entrainment can lead to renewal of cloudiness (Randall, 1984) and that cumulus convection is an important source of water for marine
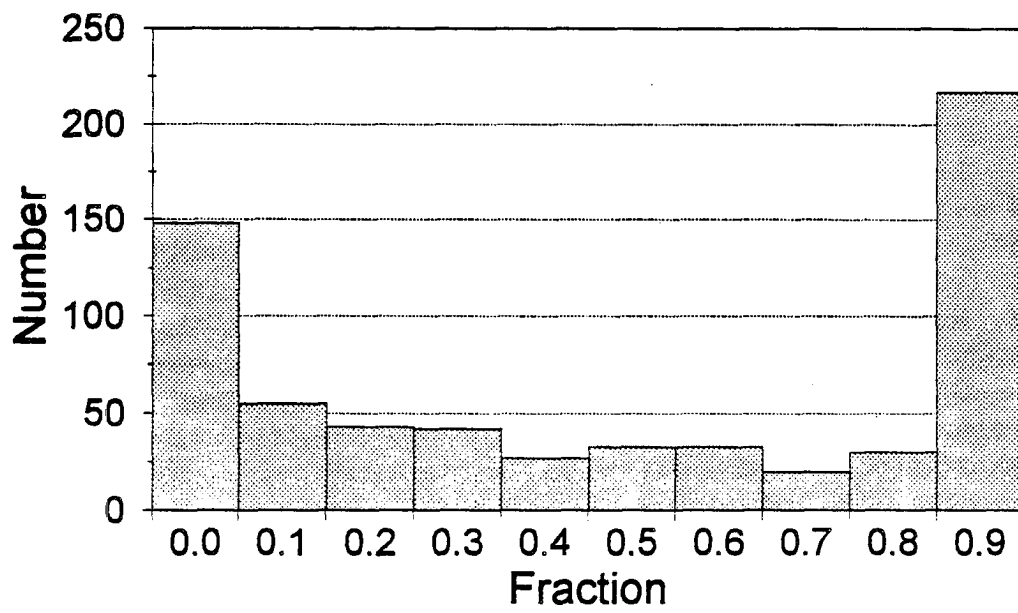
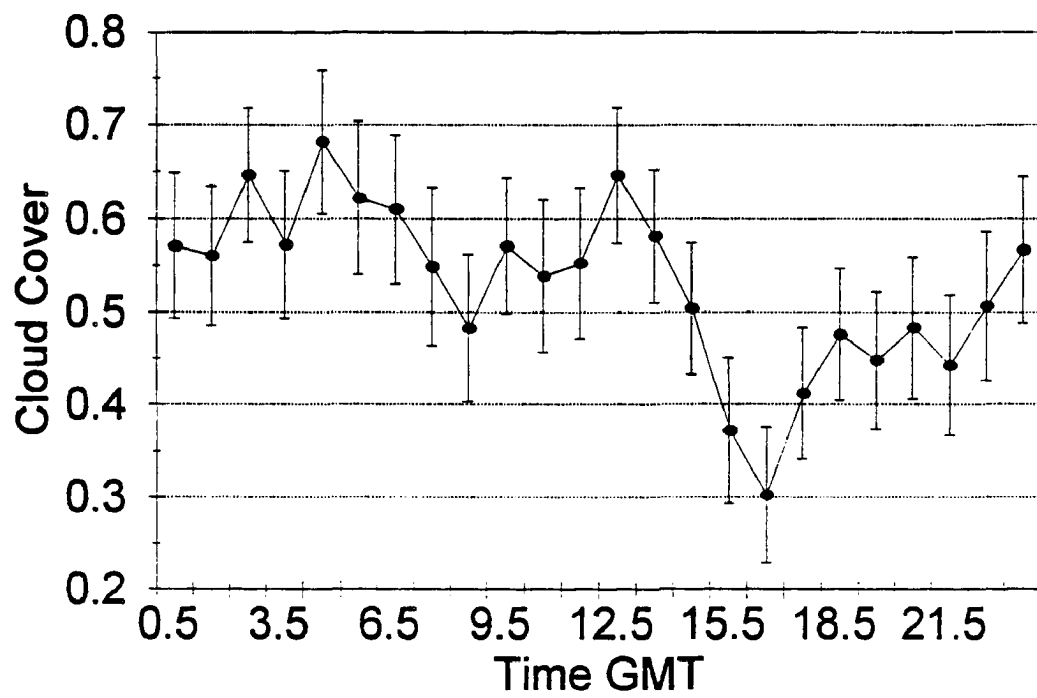Figure 2.5. Frequency of PRT-6 cloud cover

Figure 2.6. Diurnal variation of PRT-6 cloud cover

19

stratus cloud (Cotton and Anthes, 1989). A study of radiation fog, which is dynamically similar to marine stratus, by Welch *et al.* (1986) concluded that fog intensification occurs after sunrise due to increased surface evaporation and turbulent fluxes.

2.3.4 *Microwave Radiometer Measurement of Cloud Cover*

A multichannel microwave radiometer was deployed at the Porto Santo experiment site. A description of the instrument can be found in Cox *et al.* (1993a). This has provided estimates of vertically integrated liquid water and precipitable water vapor with two minute time resolution. Cloud cover has also been derived from these measurements as the fractional number of observations of liquid water in excess of a threshold. For a threshold of 0 mm, the analysis returns a mean cloud cover of 58 percent for the period of 1-28 June, 1992. Given a threshold of 0.002 mm, cloud cover is 56 percent. Given a threshold of 0.005 mm, cloud cover is 51 percent.

2.3.5 *Radar Profiles of Cloud*

An 8-mm Doppler radar was deployed at the field site by NOAA/WPL (Cox *et al*, 1993a) and the reflectivity profiles obtained by this instrument are valuable tools for examining qualitatively the structure of the boundary layer and its cloudiness. The profiles have been used to classify measurements of solar irradiance as belonging to cumulus or stratus regimes.

Chapter 3. Solar Radiation

3.1 Measurement of Solar Irradiance at the Surface

3.1.1 Geometry

The monochromatic surface energy flux density of a beam of solar radiation of magnitude I_0 incident from a zenith angle of θ_0 and a azimuth angle of ϕ_0 is

$$F_0 = I_0(\theta_0,\phi_0)\cos\theta_0 \tag{3.1}$$

The general expression for the energy flux density incident upon the surface involves an integration over the radiances in all the direction of the hemisphere such as

$$F = \int_0^{2\pi} d\phi \int_0^{\pi/2} d\theta \; I(\theta,\phi)\cos\theta\sin\theta \tag{3.2}$$

It is conventional to simplify this integral by changing to the coordinate $\mu = \cos\theta$ which yields the expression

$$F = \int_o^{2\pi} d\phi \int_0^1 d\mu \; \mu I(\mu,\phi) \tag{3.3}$$

21

The additional geometrical consideration is the approximation we will make of a plane, parallel atmosphere. That is to say, the atmosphere will be treated as a horizontally infinite slab of finite thickness which is parallel to the planetary surface, also approximated as a plane. This is a very accurate approximation for fluxes upon the planetary surface on scales and geometries such that the curvature of the earth and atmosphere are negligible.

3.1.2 Measurement of Solar Radiation

Surface solar irradiance was measured during FIRE II/ASTEX at Porto Santo by an Eppley Precision Spectral Pyranometer. This instrument directly measures the irradiance by use of a blackbody thermopile which produces a voltage proportional to the incident solar power. The accuracy of the pyranometer is typically 1 percent (Cox, *et al.*, 1993a), which translates to errors in the neighborhood of 5 W m^{-2} in the daily averaged irradiances. One pyranometer was deployed with Schott WG7 glass domes transparent from 0.28-2.8 μm and one was deployed with RG695 domes with a 0.695-2.8 μm bandpass. A pyrheliometer, was deployed on a solar tracker to measure irradiance constrained within a 5 degree field of view and allowed measurement of the energy flux density of the direct solar beam.

3.2 Solar Irradiance under Cloud-free Conditions

3.2.1 Construction of Cloud-free Dataset

The impact of cloudiness on the surface radiation budget (SRB) may be deduced by comparison of data gathered during cloudy sky conditions to data gathered under cloudless conditions. Since cloudless conditions were relatively rare, the clear sky data

are a composite of data from June 5, 7, 9, 26, and 27. The raw cloudless day data set is composed of measurements from these five days at two minute intervals between 0600 and 2010 GMT. A ninth-order polynomial was fit to this series of data and the polynomial fit serves as the reference cloudless day data set. The polynomial fit was performed to smooth out small inconsistencies between the separate data windows. By this method, four cloudless day datasets have been compiled:

1) Downward Shortwave Irradiance, 0.3-2.8 microns

2) Downward Near-Infrared Irradiance, 0.7-2.8 microns

3) Direct Solar Beam Irradiance, 0.3-2.8 microns

4) Downward Diffuse Irradiance, 0.3-2.8 microns

Datasets 1, 2, and 3 (above) have been directly measured. The fourth is derived from the difference of 1 and 3. Complementary to these data sets is the solar irradiance at the top of the atmosphere which is derived from an algorithm which computes the solar zenith, azimuth, and declination angles, and the Earth-Sun distance for any given time (Thompson, 1980). The four sets described above are shown in figures 3.1 and 3.2. Daily averages derived from the cloudless data are shown in the following table.

Table 3.1 Clear sky irradiance. 24 hour averages in the period 1-28 June 1992.

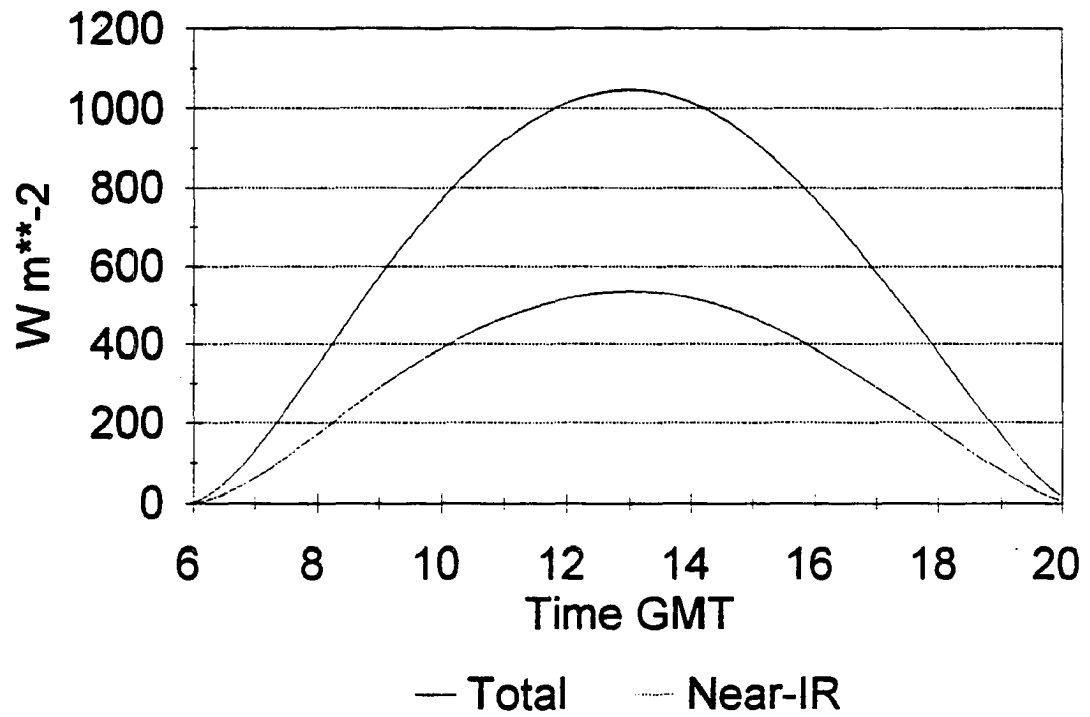| Downward Solar, surface	361 W m^{-2}
Downward Near-Infrared, surface	183 W m^{-2}
Direct Solar Irradiance, surface	288 W m^{-2}
Diffuse Solar Irradiance, surface	73 W m^{-2}

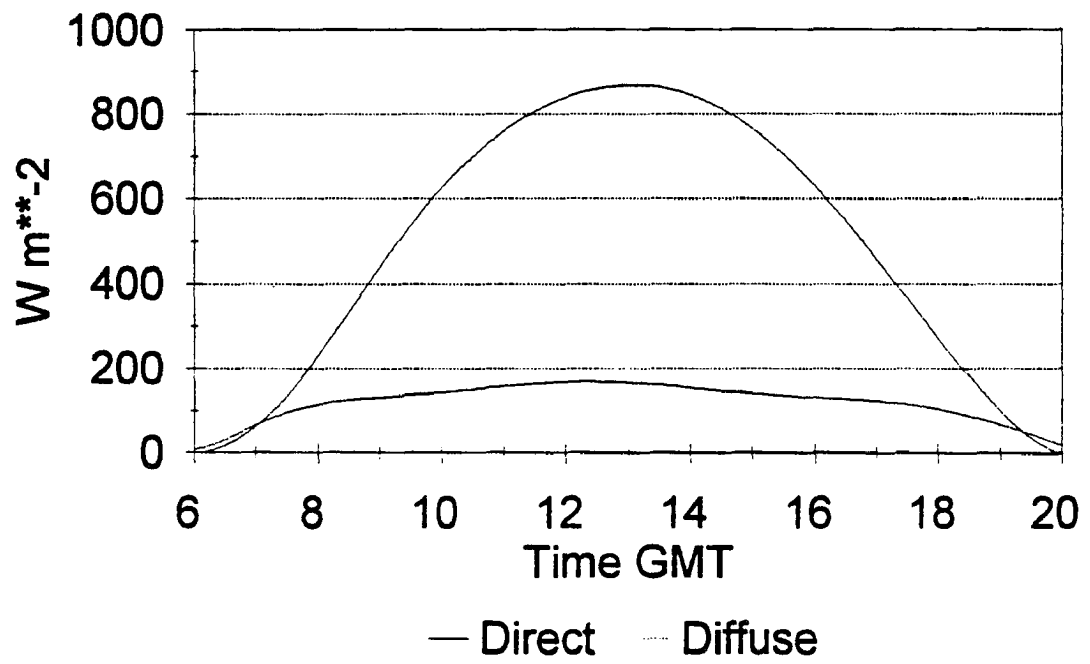Figure 3.1. Clear condition irradiance: total and near-infrared

Figure 3.2. Clear condition irradiance: direct and diffuse

3.3 Solar Radiation Budget of the Cloud-free Atmosphere

3.3.1 Solar Irradiance at the Top of the Atmosphere

An accurate assessment of the solar radiation budget begins with precise values for the extraterrestrial solar flux density and the incident zenith and azimuth angles of the solar beam. The Earth-Sun distance and solar zenith angles are calculated by an algorithm based upon the work of Thompson (1981). The annual average of the solar irradiance at the top of the atmosphere is 354 W m^{-2}. The average during the ASTEX experiment is 480 W m^{-2}. The daily averaged insolation during the IFO period is large because of the length of day and elevation of the sun. The calculated zenith angle also serves to define the limits of the daylight period which are 0600 and 2000 GMT.

3.3.2 Scattering in the Cloud-free Sky

For a typical cloudless day, 25 percent of the irradiance incident upon the top of the atmosphere is depleted by scattering and absorption, 15 percent is transmitted to the surface after scattering within the atmosphere, and 60 percent of the solar beam is transmitted directly to the surface as is shown in table 3.1. There are, certainly, scattered photons which are measured by the pyrheliometer and these are almost entirely due to an undetermined amount of boundary layer haze, however, this is a small effect and insignificant to this research. The global reflection due to Rayleigh scattering is 14-15 percent (Liou, 1992) and the diffuse transmission is of nearly the same magnitude due to the isotropy of the molecular scattering and small Rayleigh optical depth. This accounts for the measured diffuse irradiance and about 30 percent of the irradiance removed from the solar beam.

26

3.3.3 Water Vapor Absorption

Water vapor absorbs strongly in a broad band near 2.7 μm and absorbs significantly in minor bands centered at 0.72, 0.82, 0.94, 1.1, 1.38 and 1.87 μm. Liou (1992) has reported a broadband parameterization of absorption by these bands,

$$A(u_w) = f_w \left[1 - \exp\left(- \frac{11.5 u_w}{1 + 10.5 u_w + 64 u_w^{.59}} \right) \right] \qquad (3.4)$$

where u_w is the optical mass of water vapor along an atmospheric path in units of g cm^{-2} (one centimeter of precipitable water), and f_w, equal to 0.5343, is the fraction of solar irradiance in the 0.69-3.85 μm band. Vertically integrated precipitable water derived from soundings during FIRE II/ASTEX (Levy, et al, 1993) ranged from 1.5 to 3.5 cm. Broadband absorption in this range, as parameterized in equation 3.4, is shown in figure 3.3.

The precipitable water of the reference cloudless atmosphere is 2.0 cm, typical of the values observed on the day judged most nearly cloudless, June 9. To complement the values in table 3.1, the daily averaged, or global, solar absorption has been calculated. It is defined as $\bar{A} = \sum_i A_w(u_i)\mu_i F_0 / 720$, where i = 1, 2, 3, ..., 420 (the number of daylight samples), u_i is the optical mass of water vapor along a slant path, μ_i is the cosine of the solar zenith angle and F_0 is the flux density of the solar beam at the top of the atmosphere. The value obtained for $\bar{A}$ is 50 W m^{-2}. Thus, Rayleigh scattering and water vapor absorption appear to account for all the irradiance removed from the stream incident upon the top of the cloudless atmosphere, within the limits of instrumental precision.
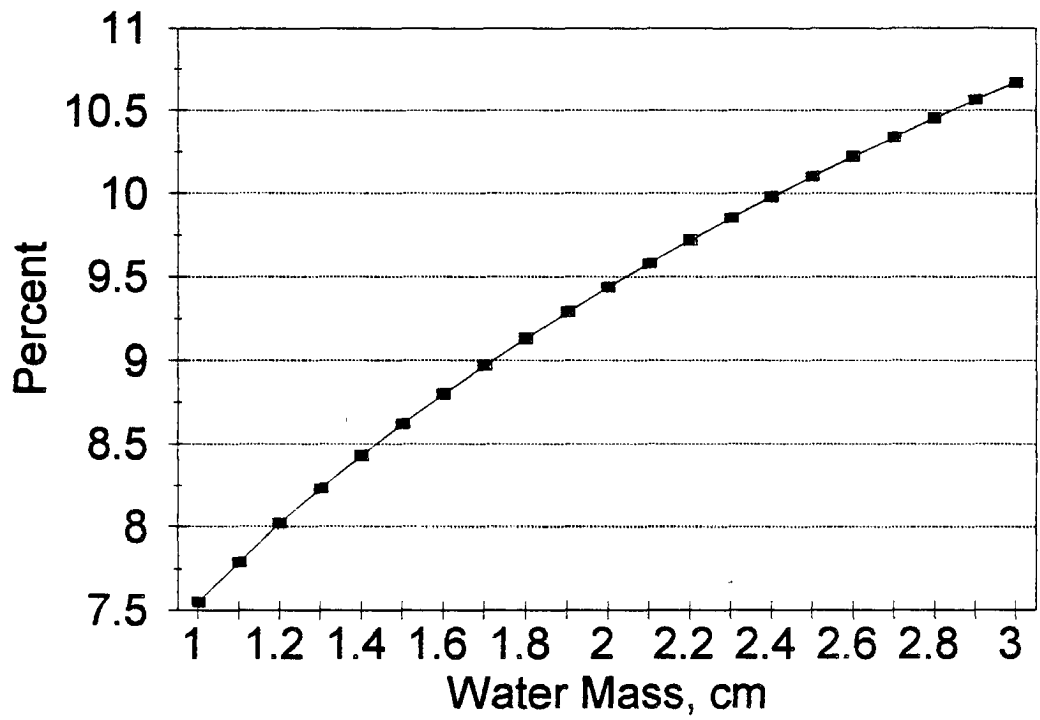
27

Figure 3.3. Solar absorption by H_2O vapor

3.3.4 Surface Reflectance

The solar radiation budget of the marine atmosphere is also affected by the reflectance of the ocean surface. Solar radiation scatters from the ocean due to interactions with suspended particles (hydrosols) and reflects specularly from the discontinuity in refractive index at the surface. Intensive observations of ocean reflectance were not part of the plan for the experiment at Porto Santo so it must be parameterized or referenced to observations from the U.K. MRF C-130 which made several flights in the vicinity of Porto Santo (Johnson, et al, 1992). In the Pinker SRB algorithm (Pinker and Laszlo, 1991), ocean reflectance is considered separately for diffuse and direct solar irradiance. The reflection of diffuse solar radiation is a constant 6 percent. The reflection of the direct solar beam (Briegleb et al., 1986) as a function of the cosine of the solar zenith angle μ_0 is expressed as

$$a^d(\mu_0) = \frac{2.6}{\mu_0^{1.7} + 0.065} + 15(\mu_0 - 0.1)(\mu_0 - 0.5)(\mu_0 - 1) \tag{3.5}$$

The value of this function is very small when μ_0 is nearly equal to one but increases rapidly as the incidence of the solar beam becomes grazing. Having determined the reflectivity of the surface and thereby the radiation upwelling from that boundary, the net solar radiation at the surface is simply expressed as

$$F_{s,net} = F_s(1 - a) = 0.94 F_s^f + (1 - a^d(\mu_0)) F_s^d \tag{3.6}$$

where F_s^f is the diffuse irradiance at the surface and F_s^d is the direct solar irradiance at

the surface. Using the cloudless direct and diffuse solar irradiances, the shortwave flux upwelling from the ocean surface is estimated to be 16 W m^{-2}. 72 percent of this radiation, 4 percent of the direct daily insolation, is reflection of the direct solar beam. Pyranometers onboard the MRF C-130 at an altitude of 100 feet measured an irradiance of 17 W m^{-2} upwelling from the ocean surface under clear skies. A consequence of the difference between the diffuse and direct albedos is that scattering elements of the atmosphere can have a small impact upon the marine surface radiation budget without necessarily reflecting radiation away from the surface. If the direct albedo were parameterized to be a constant 6 percent such as for the diffuse, one would conclude that the upwelling irradiance at the surface under cloudless conditions would have to be 22 W m^{-2}. The major terms in the cloudless solar radiation budget which have been introduced in this section are summarized in table 3.2.

Table 3.2. Components of solar radiation budget: daily averages

Solar Irradiance, top of atmosphere	480 W m^{-2}
Directly Transmitted Solar Irradiance	288 W m^{-2}
Transmission via Rayleigh Scattering	69 W m^{-2}
Reflection to Space via Rayleigh Scattering	69 W m^{-2}
Water Vapor Absorption	50 W m^{-2}
Ocean Surface Reflection	17 W m^{-2}

3.4 Solar Irradiance under Cloudy Skies

3.4.1 Geometry of Sun, Cloud, and Surface

With the possibility of overhead cloudiness, there are four possible combinations of Sun-cloud alignment, shown in figures 3.4a-d. Figure 3.4a demonstrates a case where there is no cloudiness at zenith and the direct solar beam is unaffected by cloudiness. The cloud that is present may scatter significant radiance to the pyranometer. Figure 3.4b illustrates another situation where cloudiness does not intercept the solar beam. Again, radiation may be diffusely transmitted through the cloud to the pyranometer adding to that of the direct beam. Figures 3.4c and 3.4d show cases wherein the solar beam is intercepted and extinguished by cloudiness. In 3.4c, there is no cloud at zenith while in 3.4d, there is cloud at zenith. Assumptions about the relative frequencies of these four cases must be made in the pursuit of calculating the radiative forcing of cloudiness.

Consider a case of cloudiness randomly distributed in a stratiform region where the probability of a vertical clear line of sight is ζ_0. The probability of a clear line of sight at an off zenith angle is ζ_0/μ. The frequencies of cases a and d are complementary as are those of b and c. The difference between these two sets is that c is much more likely than d because of the increased likelihood of cloudiness on a longer slanted path. In results that follow, it will be assumed, based upon the preceding argument, that case b, in which a near-horizon direct solar beam is incident upon the pyranometer although much cloudiness exists overhead is negligible.
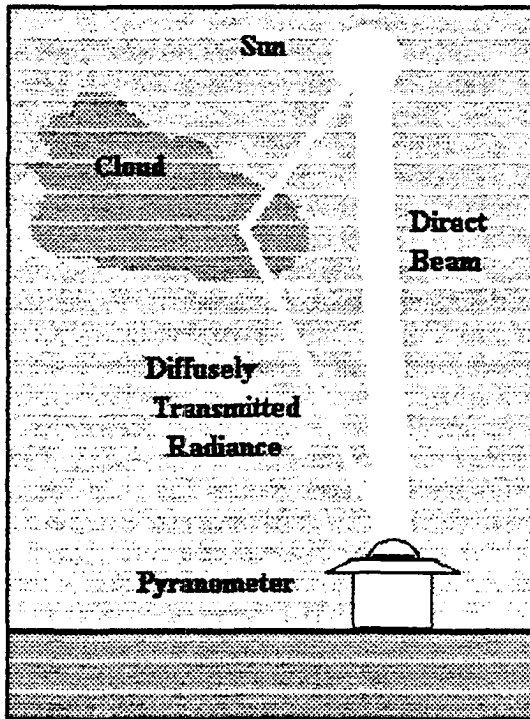
Figure 3.4a. Geometry of Sun and pyranometer in the case of cloudless zenith with cloud toward horizon.
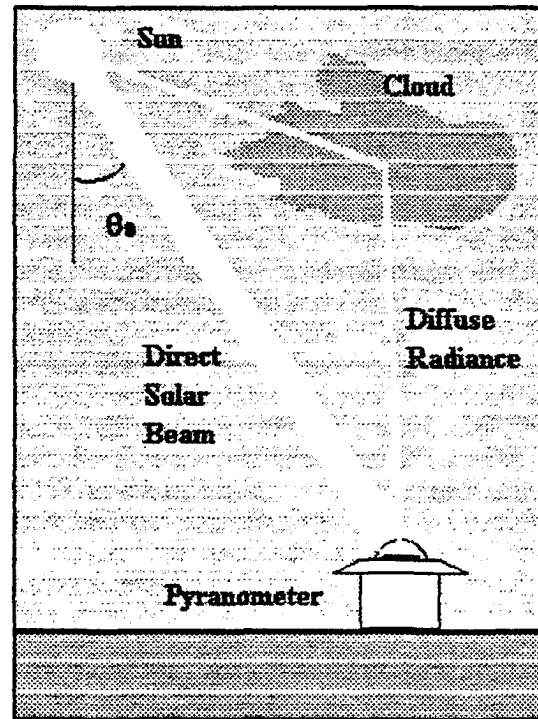

Figure 3.4b. Geometry of a case in which overhead cloudiness does not intercept the direct solar beam.
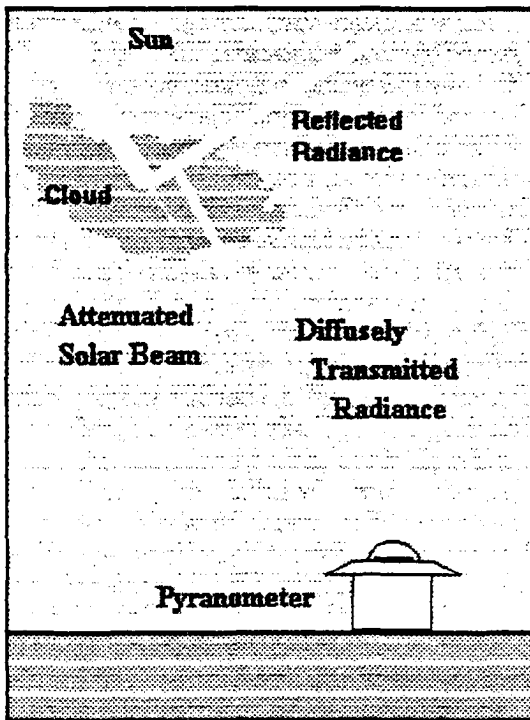

Figure 3.4c. Geometry of a case in which zenith is cloudless yet cloud obscures the direct solar beam.
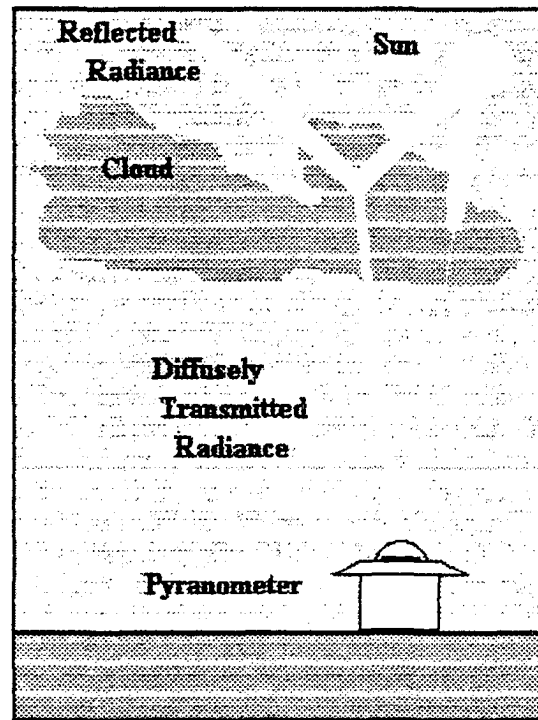

Figure 3.4d. Configuration in which cloud at zenith is intercepting and extinguishes the direct solar beam.

32

3.4.3 Deviations from Cloudless Sky Irradiance

The preceding analysis of the clear sky solar irradiance has resulted in a reference state by which one can quantify the effect of cloudiness upon the irradiance measured at the surface of the Earth. By subtracting the cloudless data from an observation, one obtains a value for the solar radiative impact of cloudiness. This presumes that clouds are the sole cause of deviations from the reference cloudless sky values. The amount of Rayleigh scattered irradiance is sensitive only to the vertically integrated mass of the atmosphere and, therefore, has fluctuations on the same order as that of surface pressure, or about 0.5 percent. Precipitable water varies within a small range (1.5-3.0 cm) and, as shown in figure 3.3, the 24 hour average absorption by water vapor varies from 46-56 W m^{-2}. This is a potential uncertainty of ± 5 W m^{-2} relative to the cloudless sky data. This value is less than the uncertainty of the pyranometer measurements and on this basis will be neglected. Since variability in Rayleigh scattering and water vapor absorption leads to a variation in downward irradiance of only $\pm$ 5 W m^{-2}, deviations from the cloudless sky values are, to good approximation, due to cloudiness. The deviation between these values shall be called the cloud radiative forcing (CRF).

Additionally, one may consider the deviation between observed and cloudless irradiance given that cloud is present at zenith (figures 3.4b and 3.4d). This quantity will be called cloud-at-zenith radiative forcing (CZRF) and quantifies the effect of cloudiness directly overhead. The CZRF is an estimate of the radiative forcing of overcast conditions, an upper bound on the impact of clouds on the surface irradiance. The presence of cloudiness is determined from the zenith 11 μm radiance, which is sampled

every 10 seconds by a PRT-6 radiometer (see section 2.2.3). 11 μm radiance is converted to a brightness temperature by inversion of Planck's Law, and cloud is judged present when a two minute average of the brightness temperature exceeds a threshold of 240 K. This threshold was chosen based upon analysis of all PRT-6 measurements (Cox, *et al*, 1993b) and will discriminate between clear sky or high cloudiness at zenith and overhead low-level cloudiness. The cloud radiative forcing (CRF) and cloud-at-zenith radiative forcing (CZRF) of the net surface solar irradiance has been calculated at two minute intervals between 0600 and 2010 GMT for each day of the experiment. Measurement of the upwelling surface irradiance under cloudy conditions when the downward irradiance equaled the IFO daily average (257 W m^{-2}) was 14 W m^{-2}. From this, it was presumed that the ocean reflectance under cloudy skies was 5.5 percent. Averages over the entire period of 1-28 June are shown in table 3.3.

Table 3.3. Total and near-infrared irradiance deviation from cloudless values

CRF, Shortwave (0.3-2.8 μm)	-102 W m^{-2}
CZRF, Shortwave	-151 W m^{-2}
CRF, Near-Infrared (0.7-2.8 μm)	-52 W m^{-2}
CZRF, Near-Infrared	-76 W m^{-2}

It is important to note that the values in table 3.3 are averages over many diurnal periods. At any given time, the deviation from the cloudless reference irradiance may be as much as -800 W m^{-2}.

The impact of cloudiness upon the direct and diffuse components of the surface solar irradiance has also been deduced. Again, the CRF is simply the diurnal average over the entire IFO period and the CZRF is the average over all measurements that coincide with the diagnosis of zenith cloud cover from the PRT-6 bolometer. The CZRF is computed from only 53 percent (see section 2.3.3) of the data points that comprise the CRF. The magnitude of the forcing is shown in table 3.4

Table 3.4. Direct and diffuse irradiance deviations from cloudless values

CRF, direct solar	-174 W m^{-2}
CZRF, direct solar	-232 W m^{-2}
CRF, diffuse solar	$+73$ W m^{-2}
CZRF, diffuse solar	$+76$ W m^{-2}

An effective cloud amount apparent in the direct solar data has been derived in the following fashion. The daily average direct irradiance was expressed as

$$F^d = F_{clr}^{\ d} + C' \cdot CRF^d \qquad (3.7)$$

and the effective cloud amount C' is 0.75. There is no meaningful cloud amount apparent in the diffuse irradiance since the CRF and CZRF are nearly equal. The cloud amount apparent in the direct irradiance data will be used to guide parameterization of cloud amount in chapters five and six.

3.4.4 Finite Cloud Effects

In the preceding section, the variable named cloud radiative forcing was associated with solar irradiance deviations measured coincident with an amount of cloudiness large enough to approximate a horizontally infinite layer. Based upon the arguments of section 3.4.2 the CZRF is representative only of the situation illustrated in figure 3.4d, cloudiness directly overhead which is extinguishing the direct solar beam. The CRF is representative of all cases which deviate from the cloudless case. The differences between these quantities would represent the effects of cases 3.4a, 3.4b (which are infrequent), and 3.4c wherein cloudiness not overhead is influencing the measured surface irradiance. This new quantity is associated with the finite size of cloud elements and is designated as finite cloud radiative forcing (FCRF).

$$FCRF \equiv CRF - CZRF .\qquad\qquad (3.8)$$

The values of CZRF reported in table 3.3 are likely to be biased and not representative of true overcast conditions. For example, consider that a single finite cloud is above the field site and is blocking the solar beam. By the methodology outlined in section 3.4.3, the solar irradiance measured under this condition would help to define the cloud radiative forcing. In this circumstance the leakage of radiation through the sides of the cloud, which still reaches the surface despite missing the instrument site, will be mistaken as cloud radiative forcing. Thus the CZRF of table 3.3 is larger than the CRF of an equivalent horizontally infinite cloud. The important implications of this bias will be discussed in later chapters.

36

Daily averages of downward surface solar FCRF are shown in figure 3.5. With two exceptions, the finite cloud forcing is positive. On days 20 and 22, the FCRF is computed from statistically insignificant number of observations. Relative to overcast conditions, the horizontal inhomogeneities of the cloud cover increase the amount of solar radiation which reaches the planetary surface.

3.5 Radiative Forcing of the Stratus and Cumulus Regimes

3.5.1 Classification

Each three hour daylight period was classified as either a stratus or cumulus regime of cloud cover to identify qualities of radiative transfer in each regime. The identification is based upon cloud reports at the time of sonde launch, the thermodynamic data from the soundings, and the reflectivity profiles from the 8 cm radar. The primary key by which the data are sorted is the cloud report. When this was ambiguous, the secondary key became the radar data. The final key was the thermodynamic profile of the boundary layer. Cloudiness regime was assumed to be stratus based upon the existence of a strong inversion in the temperature and dewpoint profiles.

3.5.2 Radiative Forcing

Cloud radiative forcing (CRF) and CZRF of the downward surface solar irradiance are averaged over 3 hour periods and then sorted by the proper regime of cloudiness. The mean forcing by cloud type over the daylight hours is shown in figure 3.6. The mean values for the IFO period are shown in table 3.5.
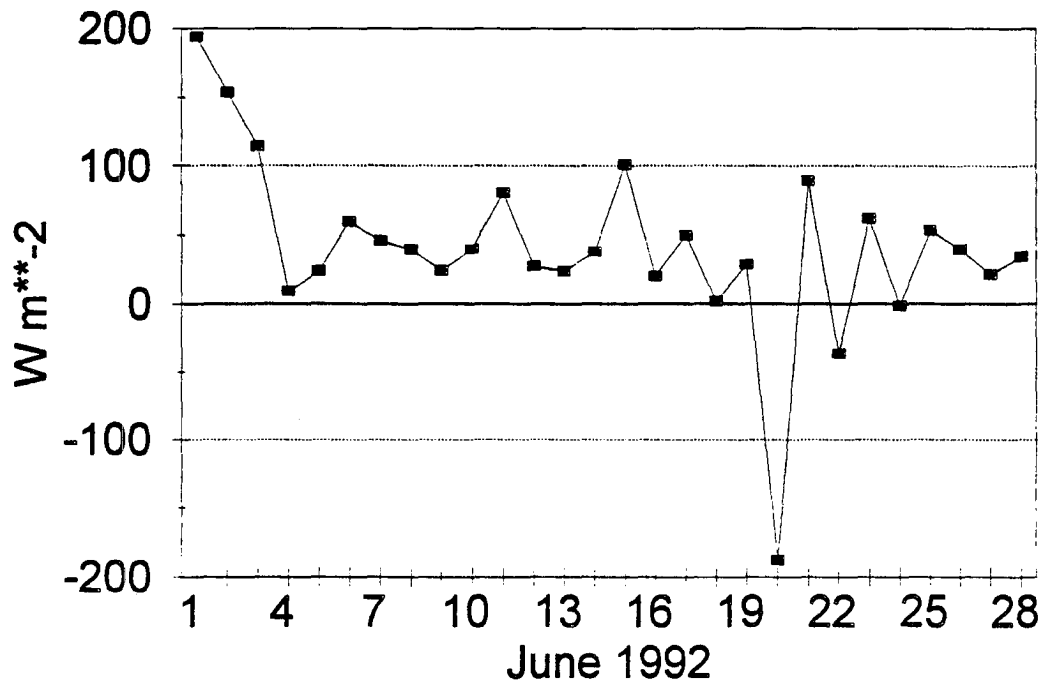
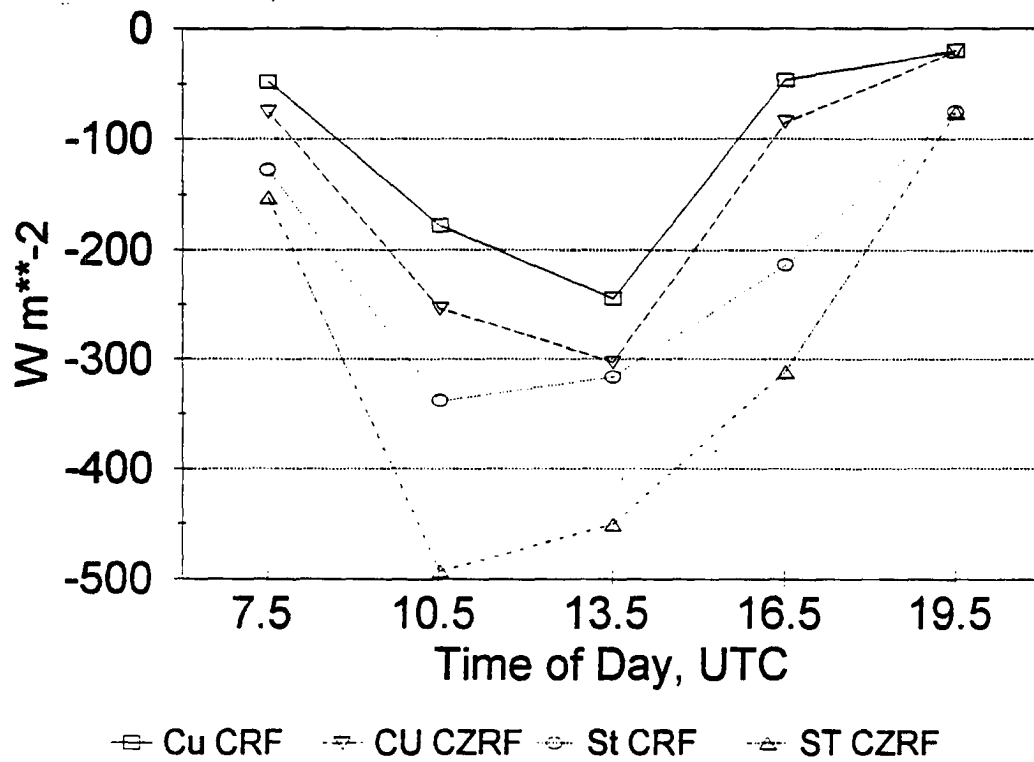Figure 3.5. Finite cloud radiative forcing: daily averages

Figure 3.7. Radiative forcing of cumulus and stratocumulus regimes

Table 3.5. Radiative forcing of cumulus and stratus regimes

Class	CRF, W m^{-2}	CZRF, W m^{-2}
Cumulus	-66	-91
Stratus, Stratocumulus	-131	-183

Chapter 4. Radiative Transfer in Finite Media

4.1 The Independent Pixel Approximation

4.1.1 Average of a Scene with Variable Brightness

The independent pixel approximation (Cahalan, 1989) is inspired by the methodologies of quantitative image analysis. A two-dimensional image is composed of many discrete picture elements, or pixels, and each pixel has a fixed and uniform brightness. If the image is of a cloud layer one might calculate the average radiance of a domain of many cloudy pixels by performing a linear sum of radiance over all the pixels within. The essential assumption is that the mean radiance is dependent only upon the number and area of pixels and is independent of their spatial arrangement. With finer resolution, meaning smaller pixels, the independent pixel approximation of the average radiance approaches the true mean radiance. The mathematical expression of this concept is

$$\bar{L}(\zeta') = \frac{\sum_{i=1}^{N} L_i(\zeta')\Delta A_i}{\sum_{i=1}^{N} \Delta A_i} \qquad (4.1)$$

41

where $L_i(\zeta')$ is the radiance coming from the ith pixel in the vector direction ζ' and ΔA_i is the area which weights the pixel's contribution to the domain mean radiance.

4.1.2 Mean Fluxes from a Scene with Variable Cloudiness

One might extend this concept to the problem of estimating the mean monochromatic radiance scattered from a horizontal domain within which optical properties are prescribed for each of a number of discrete pixels. Using the same example as in the previous paragraph, a cloud composed of water particles, given the single scattering properties (scattering and extinction efficiencies and phase function) of the particles and the vertical distribution of their number, one might estimate the radiance which is reflected upward from or transmitted through the particular pixel. Let the ith pixel's radiance be described by a function $\mathbf{H}(p_i(\zeta,\zeta'), Q_{abs;i}, Q_{ext;i}, Z_i)$ where the arguments of $\mathbf{H}$ are, respectively; the particle scattering phase function, absorption efficiency, the total extinction efficiency, and a functional representation of the pixel's microstructure. The subscript on these parameters indicates an association with a particular pixel within the domain. $\mathbf{H}$ is a generalized radiative interaction function, reflection or transmission, and serves to express the radiance scattered from a pixel in terms of the power incident upon that pixel. In the familiar case where every pixel within a scene is illuminated from the direction ζ_0 by a uniform stream of collimated radiation of flux density F_0, equation 4.1 can be written as

$$\bar{L}(\zeta') = \frac{F_0}{\pi} \frac{\sum\limits_{i=1}^{N} H(p_i(\zeta', \zeta_0), Q_{abs,i}, Q_{ext,i}, Z) \Delta A_i}{\sum\limits_{i=1}^{N} \Delta A_i}. \tag{4.2}$$

When it is the flux radiation that is of interest, it is appropriate to use a flux interaction function in the previous expression, such as

$$\bar{F}^{\pm} = F_0 \frac{\sum\limits_{i=1}^{N} H_i^{\pm}(\zeta_0, \ldots) \Delta A_i}{\sum\limits_{i=1}^{N} \Delta A_i}, \tag{4.3}$$

where $F^{\pm}$ is the upward or downward flux from the pixel after interaction with the incident beam and $H^{\pm}$ is the flux interaction function whose arguments are essentially the same as those of the bidirectional interaction function which appears in equation 4.2. The right hand side of 4.3 may be expressed as the product of the flux incident upon the scene and a mean interaction term, leading to

$$\bar{F}^{\pm} = \bar{H}^{\pm} F_0, \tag{4.4}$$

where H^+ is the quantity we recognize as the flux reflectance and H is the flux transmittance.

43

4.2 The Interaction Functions

4.2.1 Interaction of Cloud and Radiation

The problem of calculating the radiance or irradiance fields associated with a horizontally variable cloud field may be approached by resolving the cloud scene into discrete elements, or pixels in the jargon of digital image processing, within which optically active parameters are nearly homogeneous and determining a radiative interaction function for each pixel, finally summing over all pixels within the scene. Solutions to the radiative transfer equation for multiply scattering plane parallel optical media exist; the most recognized are the discrete ordinates method (DOM) of Chandresekar (1950) and the adding method of Van de Hulst (1963). The later constructs the interaction functions of an optically thick layer from a process of incrementally "adding" the interaction functions of infinitesimal single-scattering layers. These methods are only exact for horizontally infinite and homogeneous layers, *i.e.* one dimensional transport problems. Methods that consider the higher order geometries of cloudiness are used in the atmospheric sciences but are inappropriate for application within a GCM due to their computational expense and numerical instability. Methods of higher dimensional radiative transfer are, however, very useful for understanding basic differences between the interactions of finite and infinite clouds with solar radiation.

4.2.2 The Two Stream Method of Radiative Transfer

Although the two stream solutions for the radiative transfer equation have been approached from different perspectives by many authors (Meador and Weaver, 1980), it is perhaps best understood as a discrete ordinate approach using only two quadrature

angles, one in the upward and one in the downward direction. This family of solutions is computationally inexpensive and sufficiently accurate that it is a widely used method in the radiation modules of climate and numerical weather prediction models. The two stream solutions are exact only for horizontally homogeneous and infinite layers and one must well consider the consequences of using the two stream solutions to approximate radiative transfer by finite volumes of cloud.

4.3 Radiative Budget of Finite Cloud

4.3.1 First Order Approximations

The following thought experiment demonstrates much of the difference between radiative transfer in finite and horizontally infinite media. Consider a finite volume of cloud of cylindrical form, for conceptual simplicity, which is illuminated on its upper surface only by a collimated beam of radiation. Radiation exits the boundaries of the volume, or pixel, as a result of scattering processes which we will assume to be conservative. The flux density of this radiation at any boundary point x may be expressed as a sum of two terms,

$$F(x) = \bar{F} + F'(x) \qquad (4.5)$$

a constant term $\bar{F}$ and a deviation F' which is a function of position on the boundary. This problem will be approximated by assuming that the integral of the flux deviations over each boundary of the volume is zero.

Within these approximations it follows that the ratio of the flux which leaves the lateral boundaries of the cloud volume to the flux which leaves through the horizontal

45

boundaries is simply the ratio of the lateral to horizontal areas of the pixel. For the

cylindrical volume under consideration, this is stated as

$$L \equiv \frac{HorizontalOutwardFlux}{VerticalOutwardFlux} = \frac{\bar{F}\pi\,dh}{\bar{F}\frac{1}{2}\pi\,d^2} \, , \qquad (4.6)$$

and when a dimensionless parameter γ called the aspect ratio is introduced and defined

as the ratio of the pixel's vertical to horizontal scale,

$$\gamma = \frac{h}{d} \qquad (4.7)$$

we obtain the result

$$L = 2\gamma. \qquad (4.8)$$

The quantity L, which is a measure of the flux that "leaks" from the lateral sides of a

pixel, is a linear function of the aspect ratio γ. The factor of two is an artifact of the

cylindrical geometry. As a pixel becomes so wide that it is nearly horizontally infinite,

the leakage factor vanishes alongside the aspect ratio.

4.3.2 Higher Order Effects of Finite Geometry

The first order approximation evades the most challenging problems of finite cloud

radiative transfer, those of the anisotropy of radiation scattered by finite cloud and the

mutual shadowing of cloud elements. The study of McKee and Cox (1974) has provided

insight into the former problem. Their calculations of the radiative fluxes on the

boundaries of cubic clouds show that the first order approximation of section 4.3.1 is not quite true. In the case of cubic clouds with optical thickness of 4.9 illuminated at a 60 degree angle by a solar beam, it was found that the ratio of the average flux density on the cloud's sides to the flux density on the horizontal surfaces was 0.57 and the same quantity has a magnitude of 0.6 for cloud of optical thickness $\tau = 73.5$. With this in mind, the leakage that is defined in equation 4.6 should be rexpressed as

$$L = 2\lambda\gamma , \qquad\qquad (4.9)$$

where λ is the anisotropy factor that has been deduced to be approximately 0.6. This, of course assumes that the results of McKee and Cox hold as the cubic cloud is expanded horizontally. Welch, Cox, and Davis (1980) simulated scattering by finite clouds and did vary the aspect ratio of the cuboid clouds. They found a relationship between the fraction of incident irradiance which escapes from cloud sides and γ^{-1} that is nearly exponential.

4.3.3 Observed Aspect Ratios

For practical applications, the implication of the preceding analysis is that with the one kilometer horizontal resolution typical of high resolution satellite sensors (AVHRR, GOES-8), the aspect ratio of a pixel containing 500 meter thick stratocumulus is about 0.5 and the aspect ratio of a pixel containing towering cumulus several kilometers deep is 2 or greater. In the stratocumulus case, approximately one-fifth of all scattered flux is leaking from the sides of the pixel rather than being transferred vertically, and in the towering cumulus example, about half of the scattered flux exits via the pixel's sides.

The concept of an aspect ratio is also relevant to ground based radiometry. An upward-looking pyranometer, although open to a full hemisphere of radiance, has an effective field of view (FOV) that is due to the cosine response of the instrument. Sixty degrees off zenith yields half of the zenith response and will define the limit of the instrument's FOV. When observing the flux downward from a cloudy layer which has a cloud base height of 1000 meters, typical of the subtropical marine boundary layer, the pyranometer is effectively seeing a pixel that is four kilometers in diameter. Assuming the cloud layer is 500 meters thick, the pixel aspect ratio is about 0.125. According to the relationship expressed in equation 4.8, a significant amount of the solar radiation incident upon the pixel may leak horizontally and be missed by the pyranometer. For a stratocumulus filled pixel, approximately six percent of the scattered radiation leaks and for a pixel filled with cumulus, the leakge is four times greater. Radiation may reach the pyranometer from pixels adjacent to the one directly overhead but their cosine-weighted power is small, therefore, while a finite cloud transmits more radiation per unit area than an equivalent infinite cloud, a single pyranometer measurement is affected to some extent by the leakage and may lead to overestimates of cloud radiative forcing. From the previous work of Welch, *et al* (1980), it is estimated that the fractional leakage from the discrete sky volume within the FOV of a upward looking pyranometer is within 10-15 percent.

4.3.4 Ensembles of Finite Clouds

Considered in isolation first, the finite volume is actually embedded in a larger ensemble of pixels and its neighbors do impact the radiative energy budget of the pixel.

Now, in addition to the collimated source, the pixel receives a flux of energy through its lateral boundaries. A fraction of this flux will subsequently leave the pixel through its horizontal boundaries and the result is an increase in the radiance upwelling from the pixel. This first order analysis of radiation leakage from a finite volume of cloud produces the expectation that an isolated finite cloud will appear less bright (in terms of the nadir or zenith scattered radiance) than the same cloudiness when embedded in a larger ensemble of cloud.

4.3.5 Ensemble Averaged Edge Errors

The expectation, based upon the preceding first order analysis, is that a finite pixel will reflect and diffusely transmit less radiation in the vertical per unit area than a horizontally infinite cloud of the same composition. The difference is an edge effect, radiation "leaks" from the sides of a pixel. For this reason, a downward looking pyranometer deployed just above an isolated finite cloud will measure a lower flux density than if the cloud were infinite. Using the two stream solutions for a finite cloud pixel will result in a significant error in the radiation budget of that pixel but one is primarily interested in the radiation budget of a larger domain composed of many pixels. The global leakage error will be smaller than one expects from a single pixel because of mutual leakage. For example, consider a horizontally homogeneous and infinite domain to be composed of many identical cloudy pixels. The two stream solutions will overestimate the vertical fluxes on the boundaries of an isolated pixel (in the absence of the others) but when one integrates over the entire domain, the errors must sum to zero. Cahalan, et al (1994) claim that the net leakage error is less than one percent when the

variability in cloud optical thickness is constrained to sufficiently large scales. Practically, this condition will be met when the contrast in optical thickness between adjacent pixels is small. This condition is generally met in real clouds (Cahalan et al, 1994), and also is independently validated by the study of McKee and Cox (1974), who reported that under zenith sun conditions the fraction of incident light which exits the sides of a cubic cloud varies with optical thickness only between 50 to 70 percent. One may expect then, that flux gradients in an ensemble of pixels are smaller than the gradients of optical thickness. It appears that the independent pixel approximation using one dimensional radiative transfer solutions is a valid method for estimating the mean fluxes of a variable domain.

One additional complication remains, and this is the finite sampling of the cloud ensembles. In the following chapter, developement of a parameterization for ensemble-averaged properties will exploit an assumption of a infinitely large and isotropic ensemble. This situation can not be found in the atmosphere. Poellot and Cox (1975) addressed this issue and came to the conclusion that a sampling time of hours is required to accurately estimate the true mean downwelling solar irradiance from an inhomogeneous cloud field. Unfortunately, the state of the atmosphere can change significantly within the necessary sampling time, rendering the task impossible. Therefore, ensemble leakage errors are likely to persist in hourly-averaged irradiances.

Chapter 5. Parameterization

5.1 Mean Optical Properties of a Variable Domain

5.1.1 Independent Pixel Approximation

Within this chapter we will apply the independent pixel approximation to obtain a best estimate of the average reflection and transmission of an extended and variably cloudy layer. Assuming that the layer can be resolved into N discrete elements, which we will continue to refer to as pixels, the domain mean reflection is expressed as

$$\bar{R} = \frac{\sum\limits_{i=1}^{N} R(\tau_i)\Delta A_i}{\sum\limits_{i=1}^{N} \Delta A_i} \quad . \tag{5.2}$$

The analysis contained within this chapter will focus upon the parameterization of optical thickness variability only. The radiative properties of thick clouds in the Earth's atmosphere are primarily functions of the degree of multiple scattering and this makes the vertically integrated extinction the most important parameter to consider. Two stream solutions of the radiative transfer problem will be used to calculate each pixel's contribution to the mean. The domain shall be extended to be horizontally infinite and

51

variable so that the individual pixels are of a sufficiently small aspect ratio that their individual and ensemble average leakage is negligible. Under this assumption we can transform equation 5.1 into an integral form,

$$\bar{R} \equiv \int_0^\infty \zeta(\tau) R(\tau) d\tau \ .$$ (5.2)

Independency of the pixels allows one to collect all pixels of identical optical thickness. Cloud optical thickness is now treated as a random variable in the domain and is distributed according to the probability density function, *pdf*, $\zeta(\tau)$.

5.1.2 *Gamma Distribution of Optical Thickness*

A useful pdf, and one that is supported by observation, is the gamma distribution,

$$\zeta(\tau) = \frac{\lambda e^{-\lambda \tau}(\lambda \tau)^{s-1}}{\Gamma(s)} \ .$$ (5.3)

This is a distribution with two parameters, λ and s. The mean and variance of the gamma distribution can be expressed as functions of the parameters,

$$\bar{\tau} = \frac{s}{\lambda} \ ,$$ (5.4)

$$\sigma_\tau^2 = \frac{s}{\lambda^2} \ .$$ (5.5)

52

This allows the pdf to be rewritten in terms of the mean and variance parameter of the distribution,

$$\zeta(\tau;s,\bar{\tau}) = \frac{\frac{s}{\bar{\tau}}e^{-\frac{s}{\bar{\tau}}}(\frac{s\tau}{\bar{\tau}})^{s-1}}{\Gamma(s)} \ . \tag{5.6}$$

The form of the gamma pdf is shown in figure 5.1 for several values of the shape parameter s. Each distribution has the same mean optical thickness.

5.1.3 Observed Distributions of Liquid Water Path

Measurements of integrated liquid water, although rare, suggest that the gamma distribution is an appropriate model for the subgrid scale variability of liquid water path and cloud optical thickness. Distributions of liquid water path reported by Wielicki and Parker (1994) also support the use of a gamma distribution for liquid water path (figure 5.2), as the gamma distribution can model both the nonmodal distributions they report for sparse cloud and the peaked distribution within overcast sky with the proper gamma distribution shape parameter. The daytime distribution of liquid water path measured by the NOAA-WPL microwave radiometer during the ASTEX/FIRE II IFO is also supportive of a gamma distribution. Figure 5.3 shows the IFO distribution of W and a gamma distribution with the same mean and variance. The gamma distribution does not account for some cloudiness between 5-25 g m^{-2} and contains too much of the most wet (W > 100 g m^{-2}) cloud but is otherwise in agreement with the data.
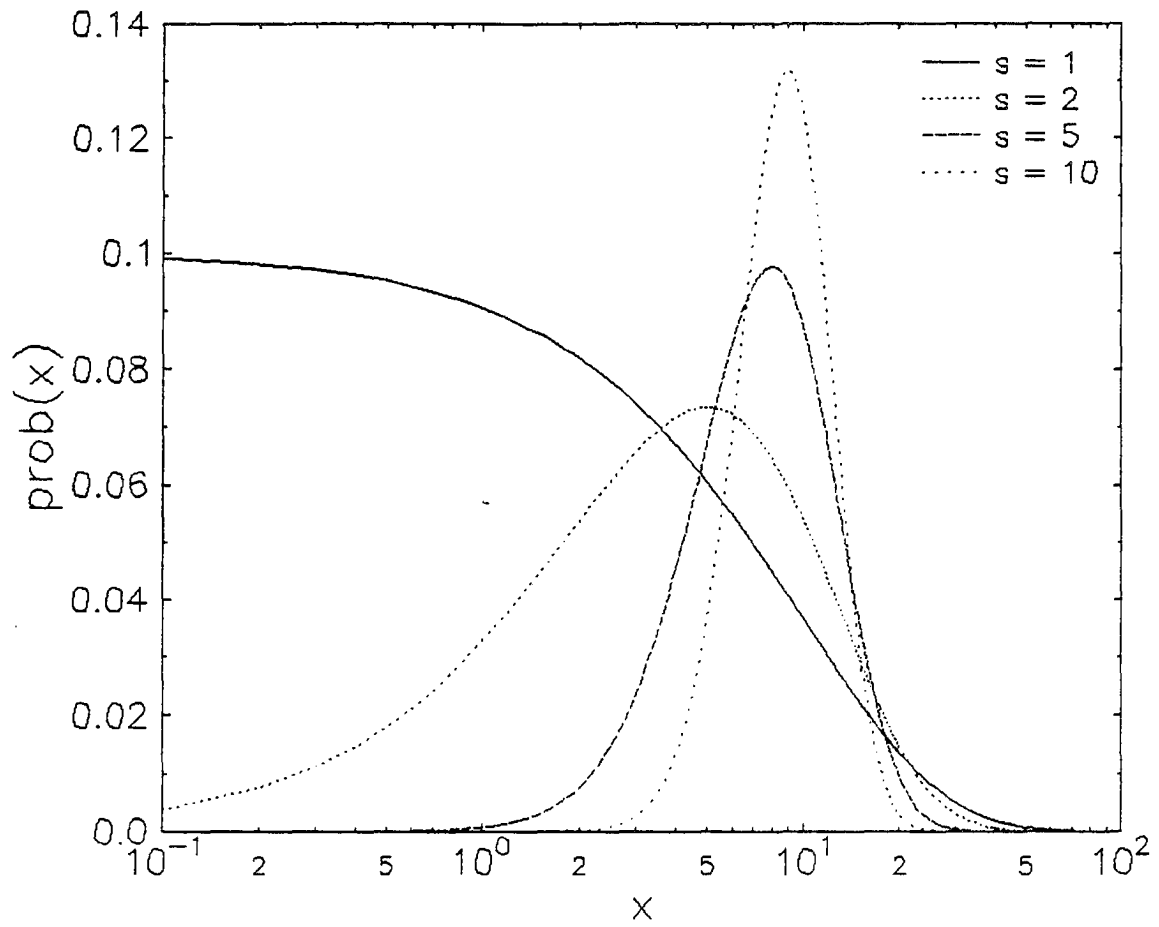
Figure 5.1. Gamma distribution function illustrated for several shape parameters
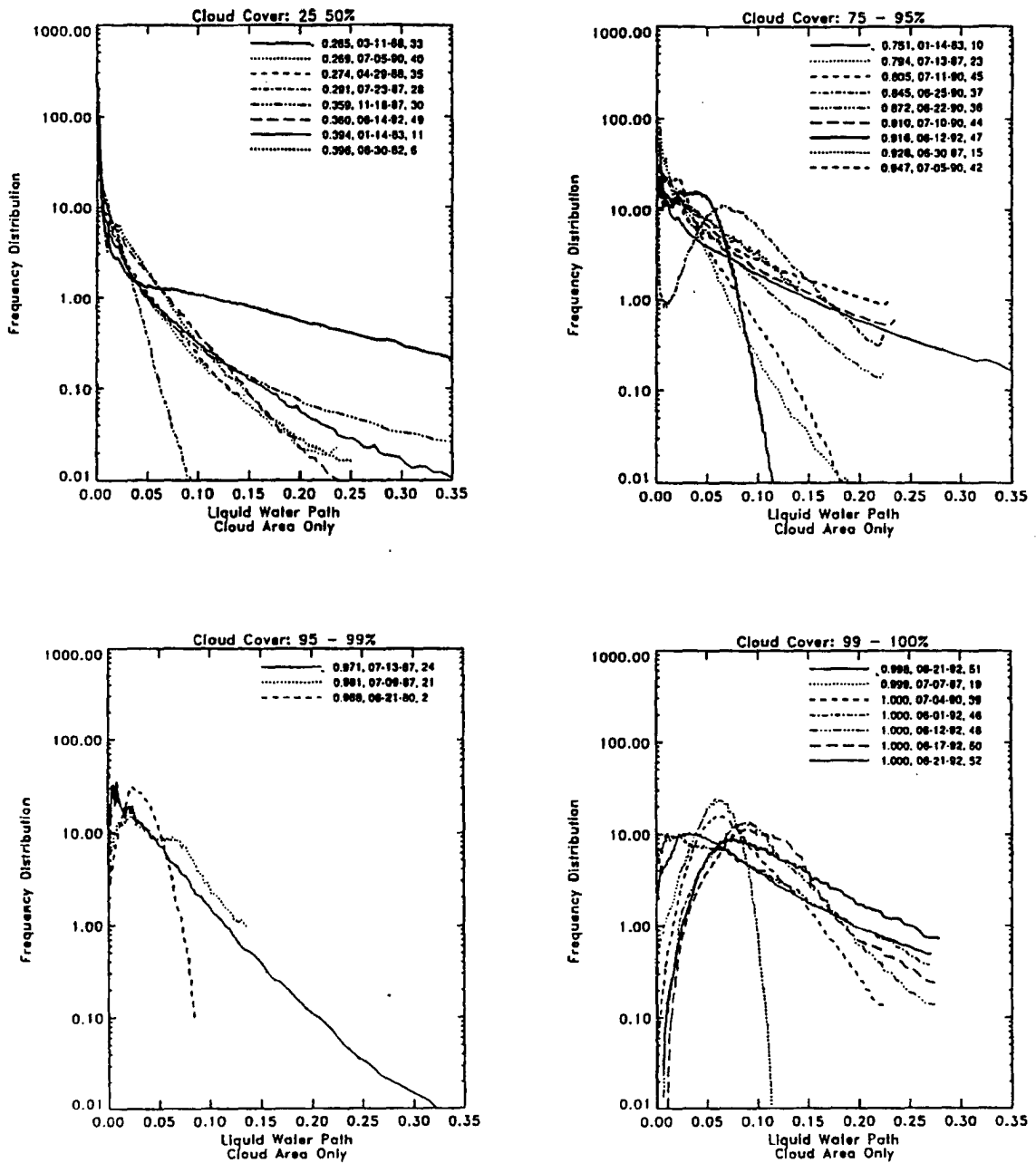
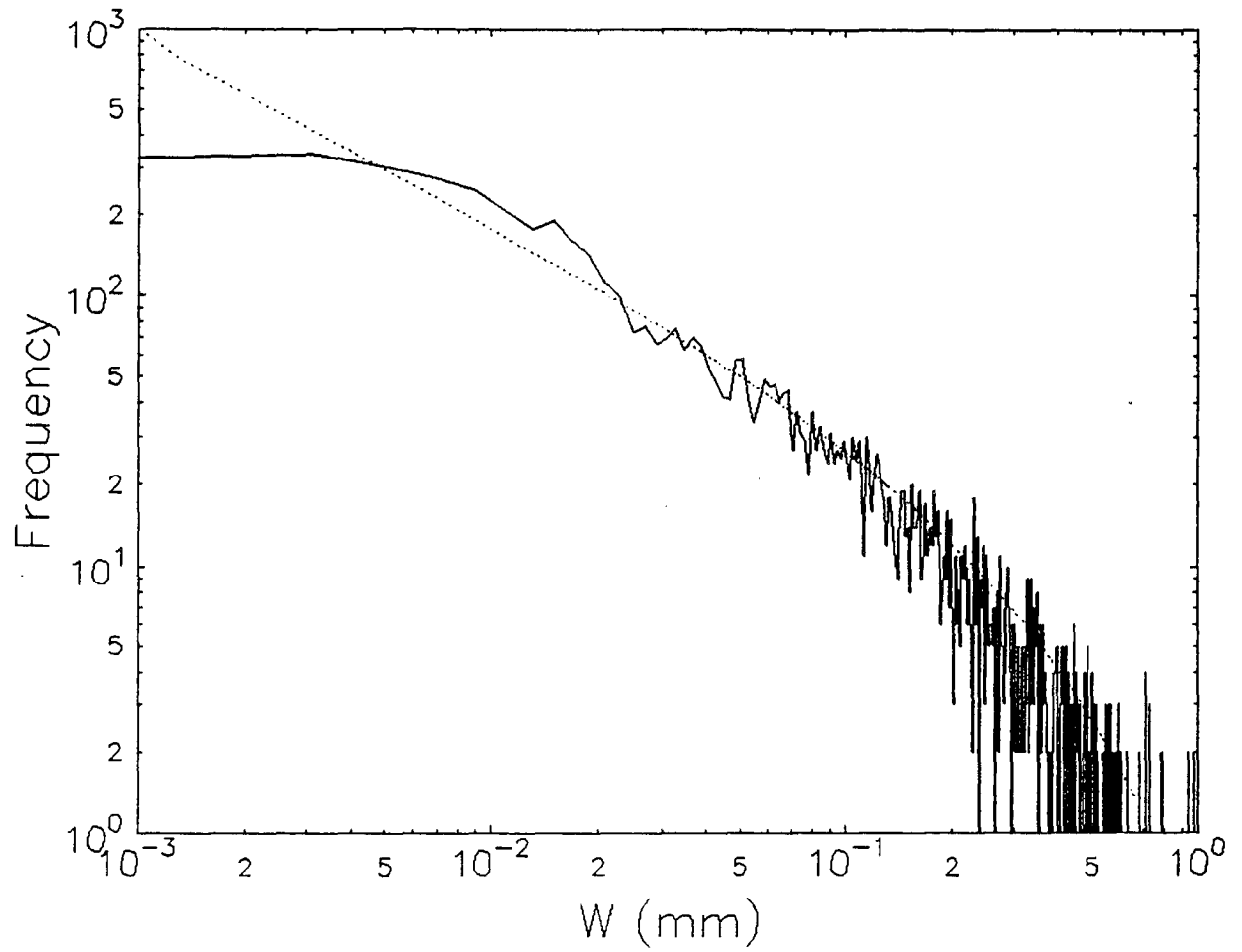Figure 5.2. Liquid water path distributions from Landsat. From Wielicki and Parker (1994).

Figure 5.3. Comparison between gamma distribution and LWP distribution. Solid line is the observed LWP, dashed line is a gamma distribution of same mean and variance.

58.1.4 Numerical Integration

The answer to the integral equation 5.2 is obtained by solving, for $\bar{R} = r(\infty)$, the associated ordinary differential equation

$$\frac{dr}{d\tau} = \zeta(\tau)R(\tau) ,\qquad (5.7)$$

with the boundary condition $r(0)=0$, by a fifth order Cash-Karp Runge-Kutta method with an adaptive step size (Press et al, 1992). Figure 5.4 illustrates the accuracy of this method when applied to the integration of the *pdf* alone. The integrated probability of the distribution must be one and the errors are less than 0.001 for a wide range of mean and variance.

5.1.5 Albedo Bias

The quantity δR which is defined as

$$\delta R \equiv R(\bar{\tau})-\bar{R} ,\qquad (5.8)$$

is contoured in figures 5.5a-d. This is the difference between the reflectance of a homogeneous cloud and the IPA reflectance of a variable cloud with the same mean optical thickness. The error is strictly positive under the independent pixel approximation due to the convexity of the reflection function (Cahalan, 1994). The bias is shown for two representative wavelengths, one visible (conservative scattering) and one near-infrared (single scattering albedo of 0.99), and two solar positions; a zenith sun and $\theta_0 = 53.2$ degrees (the IFO daily average solar position). There is a ridge-like feature in the near-

57
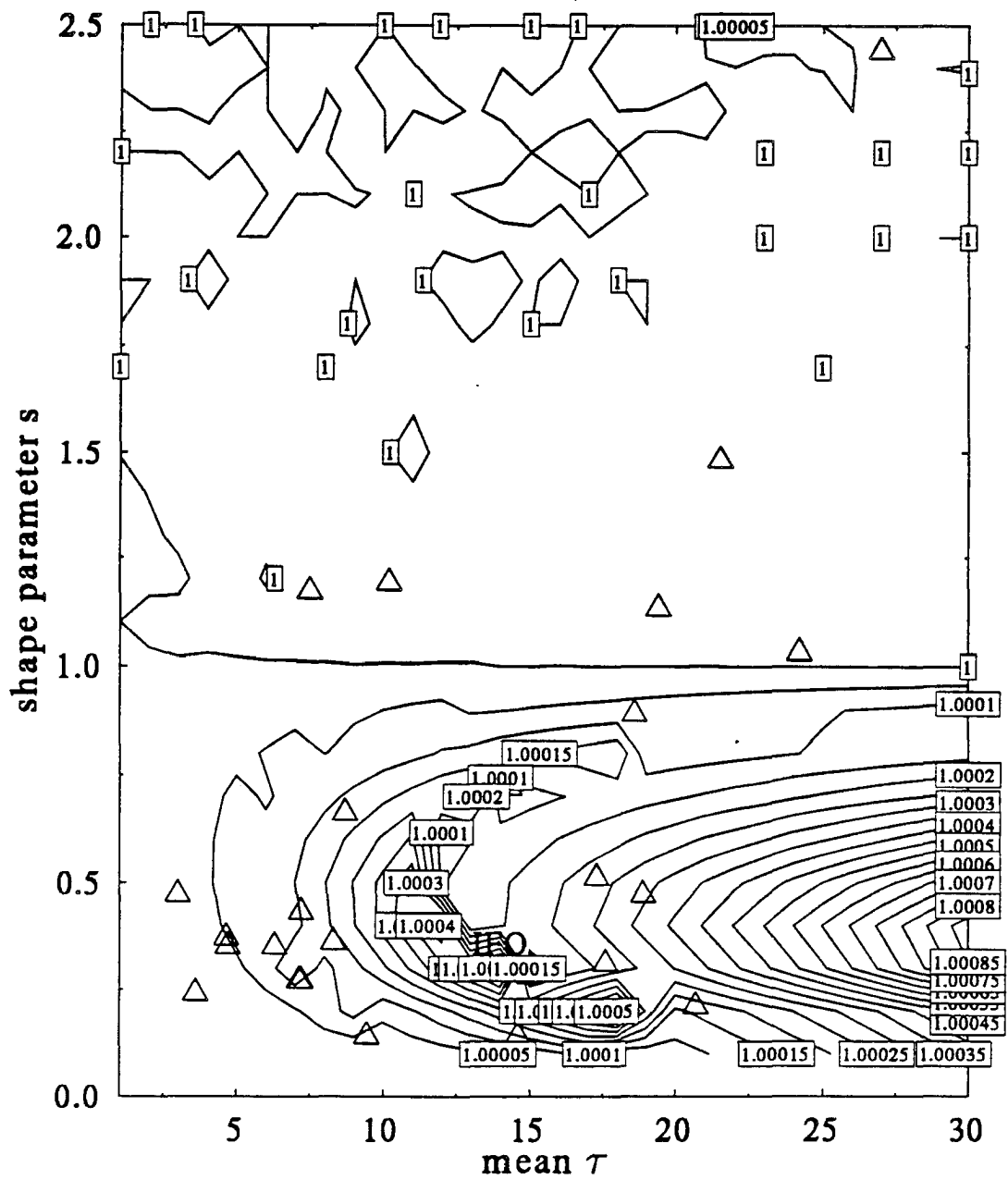
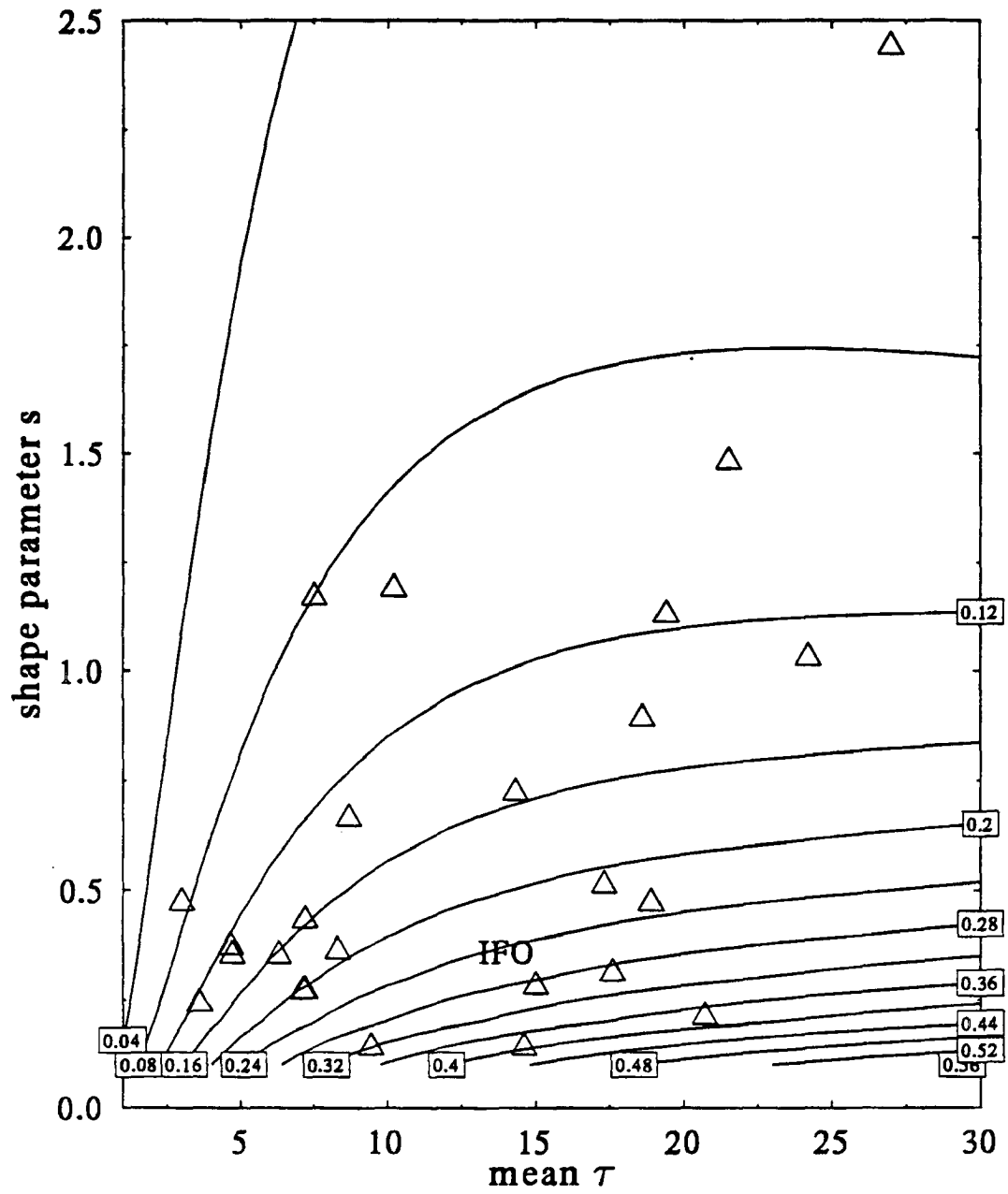Figure 5.4. Numerical integration of the gamma distribution function

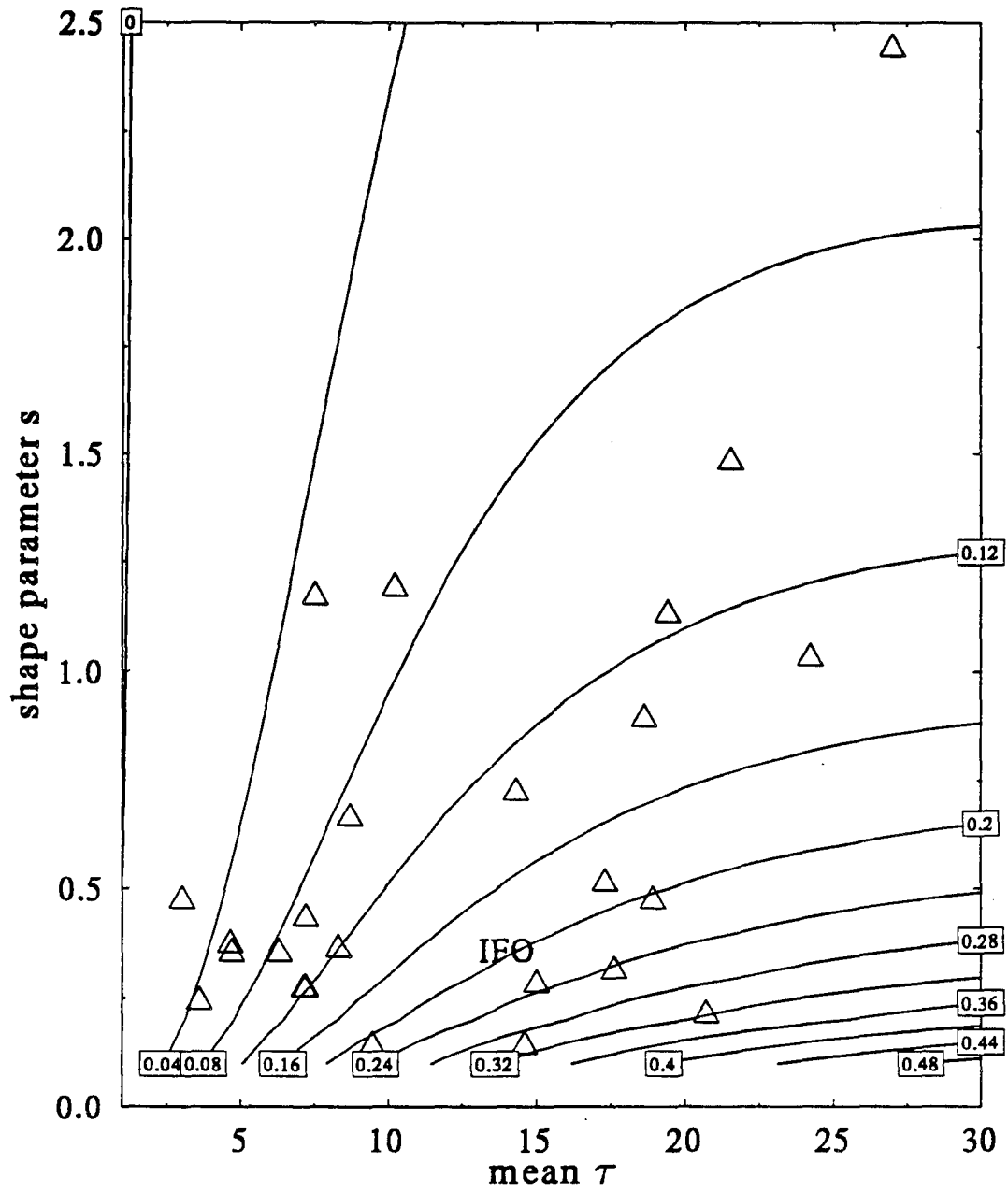Figure 5.5a. Reflection error: visible wavelength, low sun

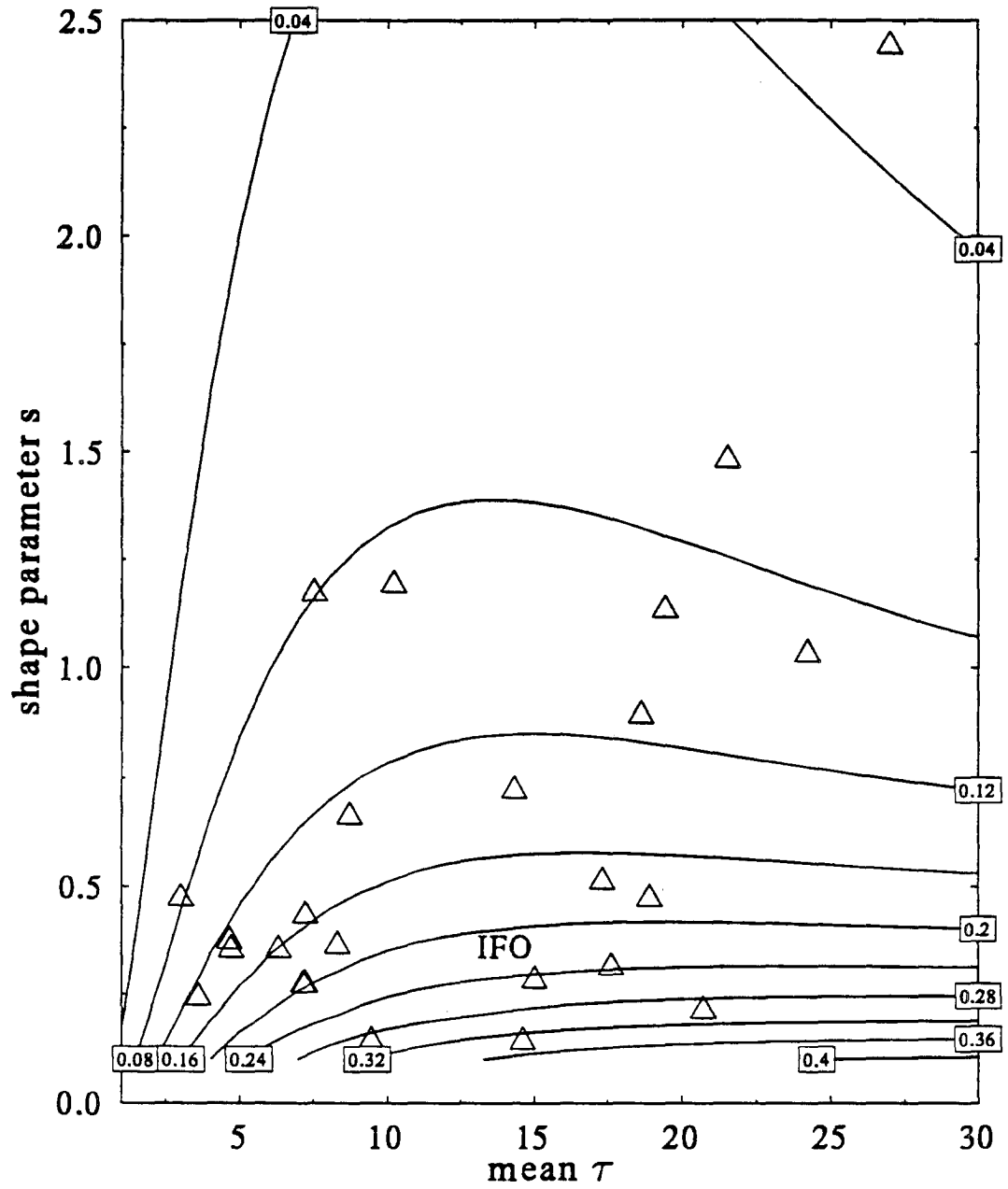Figure 5.5b. Reflection error: visible wavelength, zenith sun

60

Figure 5.5c. Reflection error: near-infrared wavelength, low sun
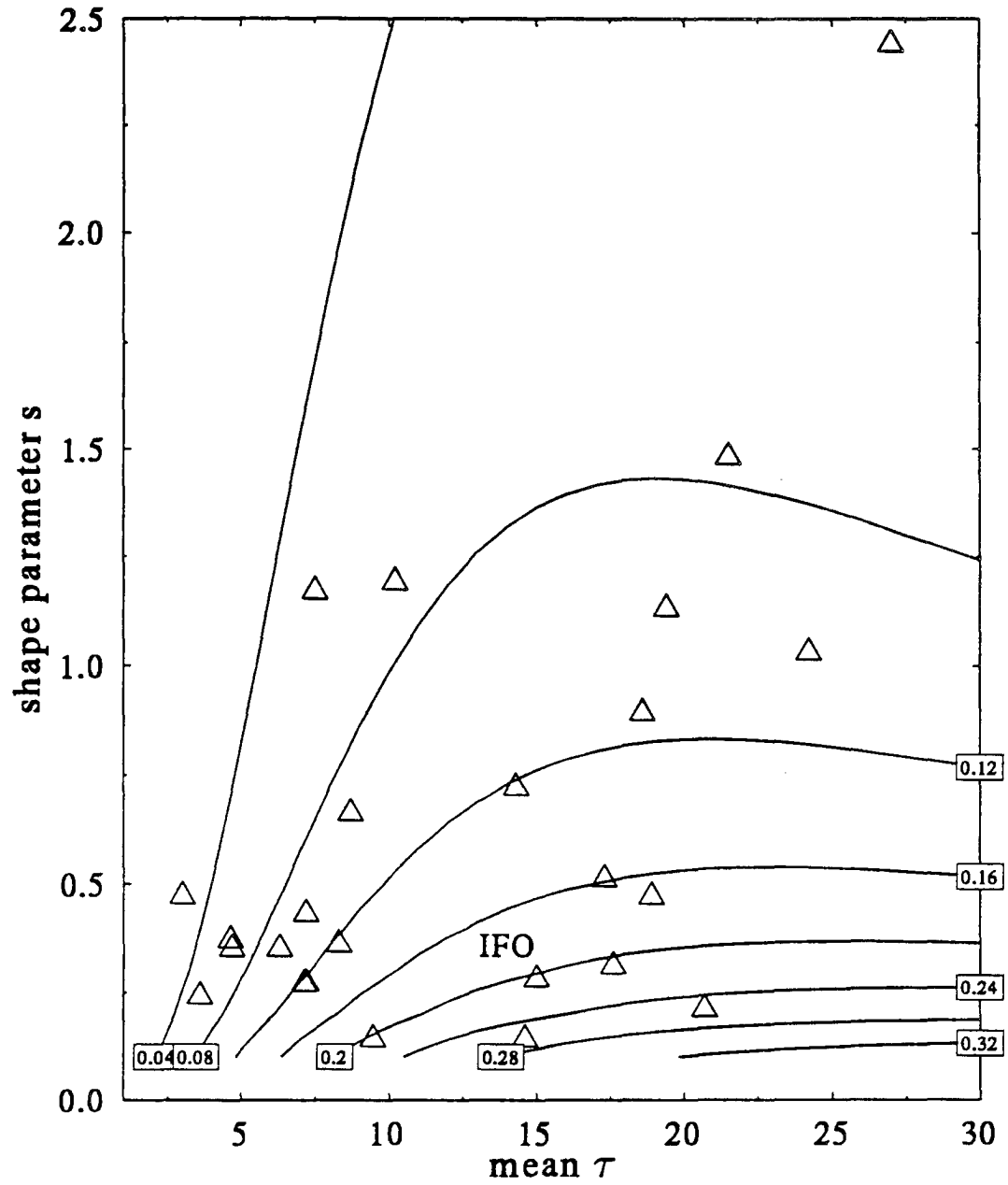
61

Figure 5.5d. Reflection error: near-infrared wavelength, zenith sun

infrared contours (figures 5.5 c and d) because absorption in the more optically dense portions of the cloud layer reduces the albedo bias. The ridge does not appear in the visible contours (figures 5.5 a and b) and the albedo bias increases monotonically with mean optical thickness and increasing variance. The albedo bias for a gamma distribution characteristic of the daytime liquid water path during the entire ASTEX IFO (the triangle labelled 'IFO') is at least 0.2 for the four scenarios. The cloudiness observed on June 17, 1992 was the most nearly overcast but still falls into the neighborhood of a 10 percent absolute albedo bias.

5.1.6 Transmission Bias

Figures 5.6 a-d show the results of a complementary analysis of the domain mean transmission. The transmission bias is negative.

5.2 Relative Error and Reduced Optical Thickness

5.2.1 Relative Reflection Errors

Additional insight is obtained by examining contours of the relative reflection bias

$$\Delta R \equiv \frac{R(\tau) - \bar{R}}{\bar{R}} . \tag{5.9}$$

Figure 5.7 shows contours of the relative reflectance error for a visible wavelength and the ASTEX daylight-mean solar angle. Based upon these data, the relative albedo error will be parameterized as
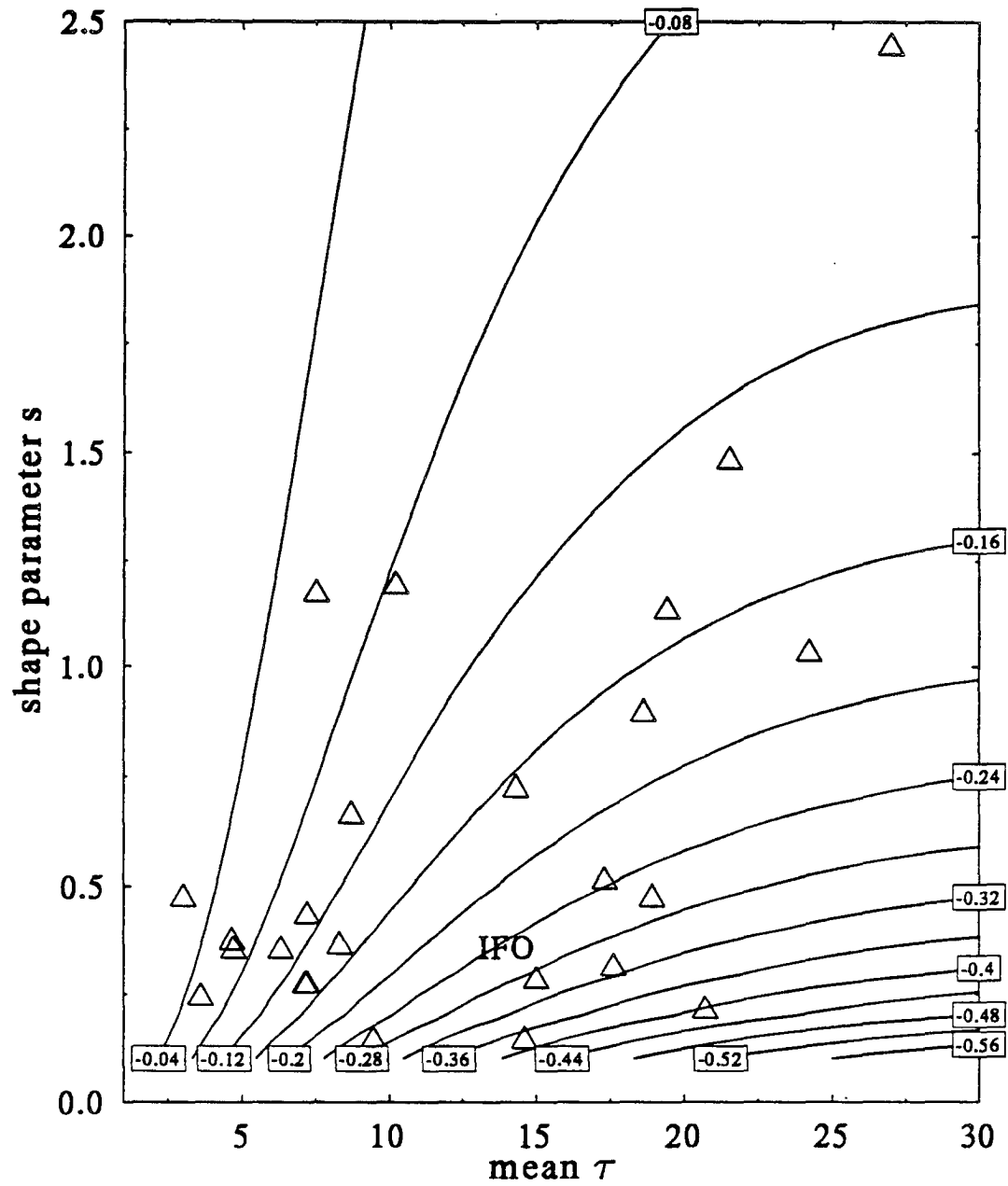
Figure 5.6a. Transmission error: visible wavelength, low sun
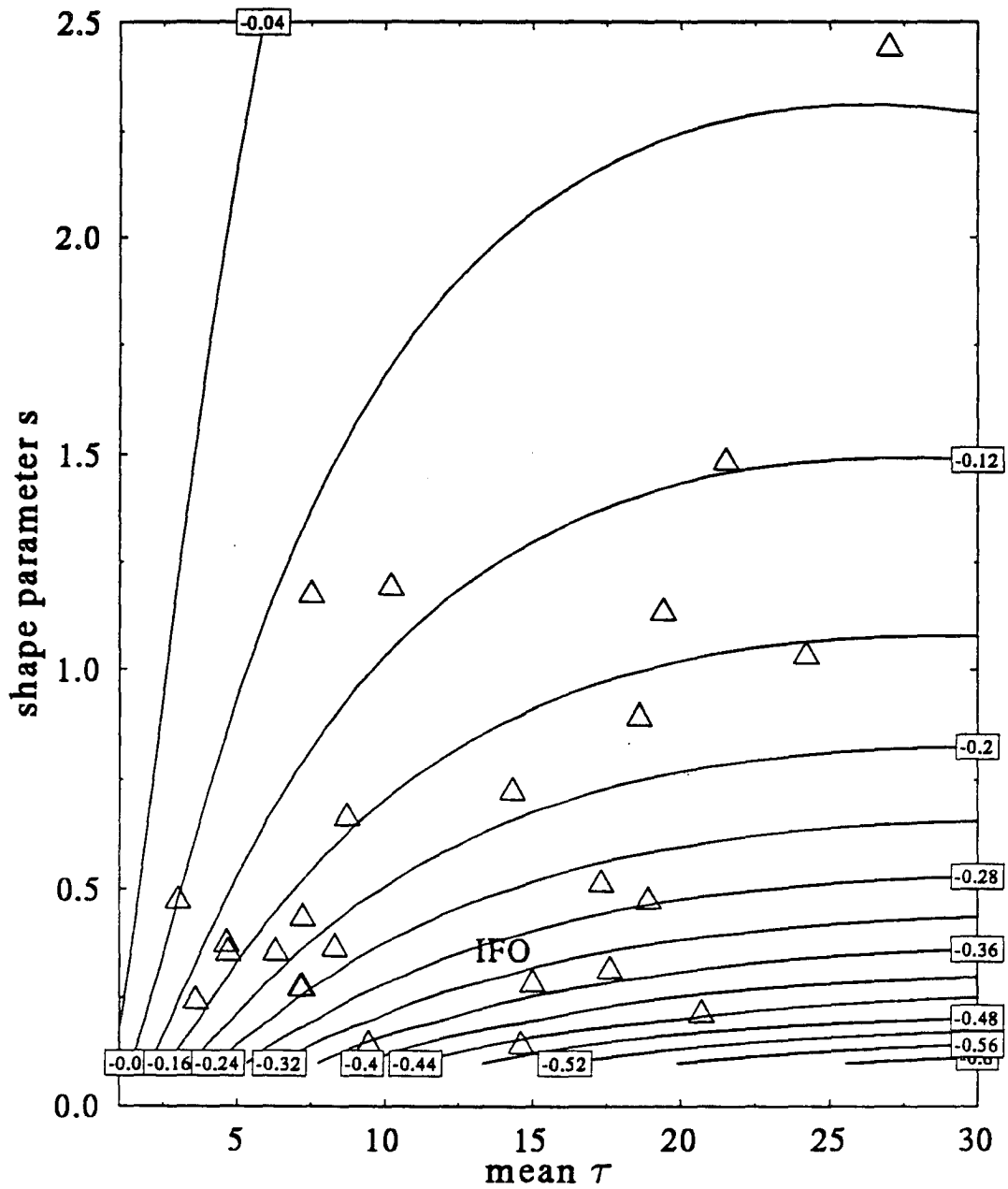
64

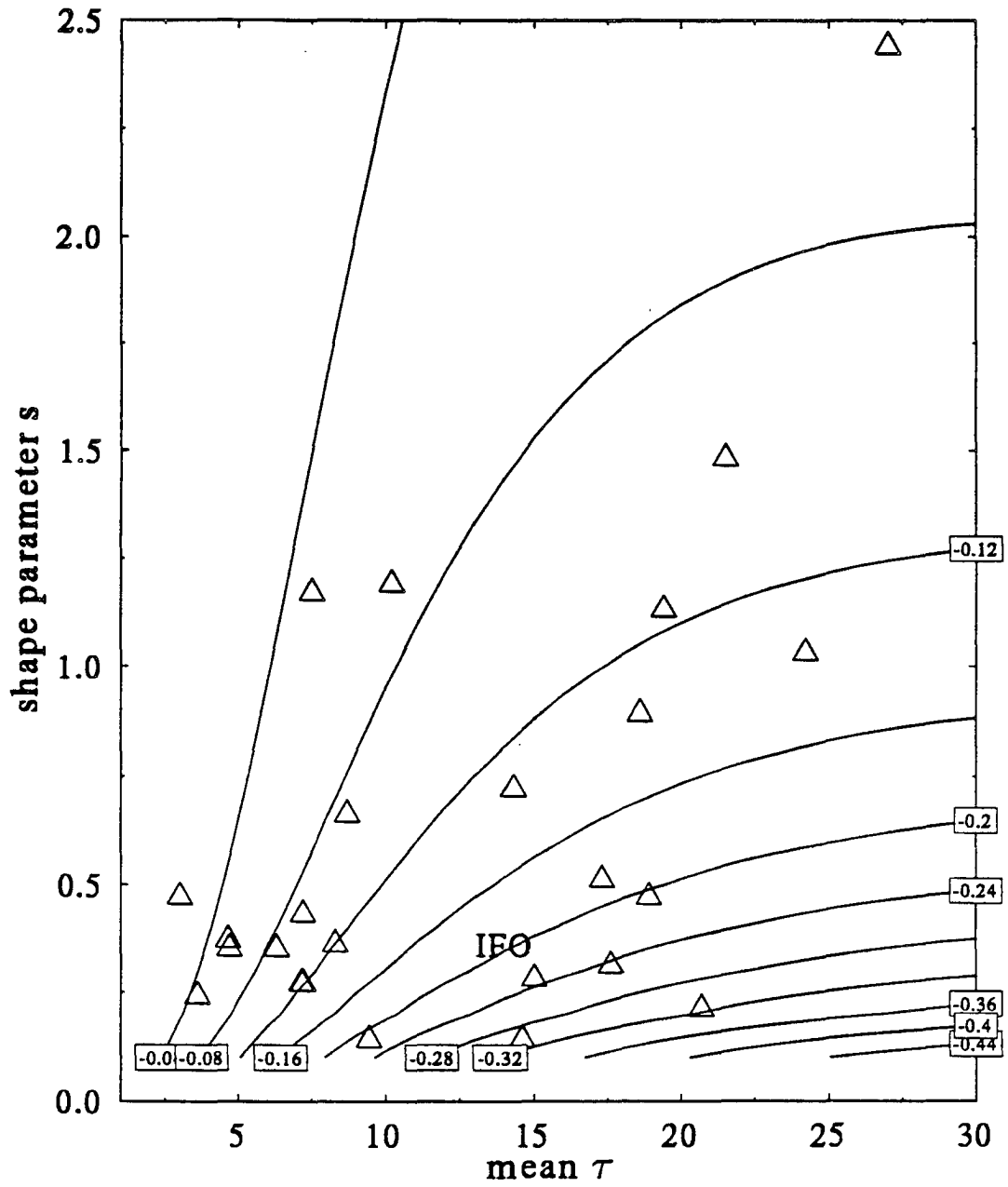Figure 6.6b. Transmission error: visible wavelength, zenith sun

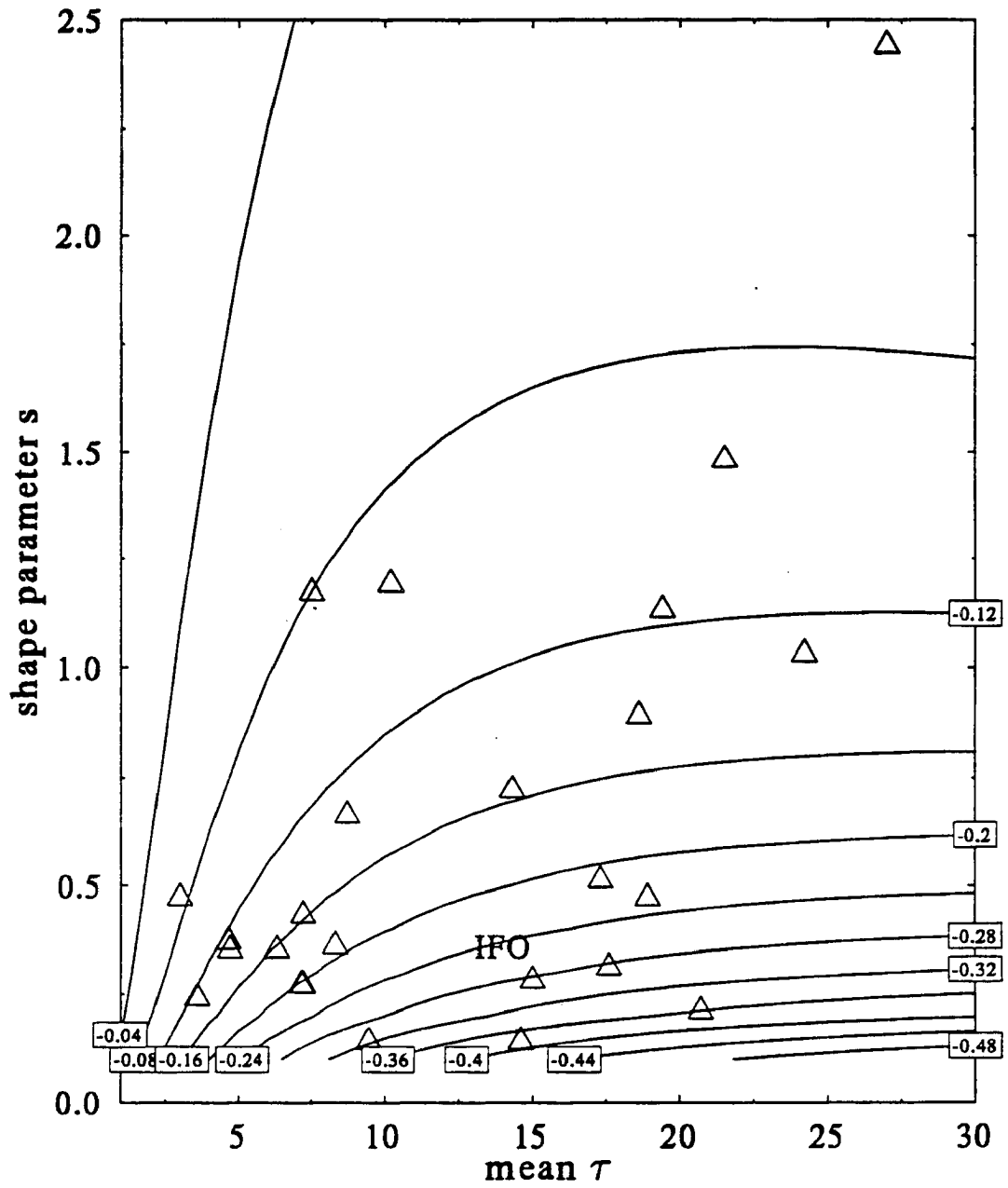Figure 5.6c. Transmission error: near-infrared wavelength, low sun

Figure 5.6d. Transmission error: near-infrared wavelength, zenith sun
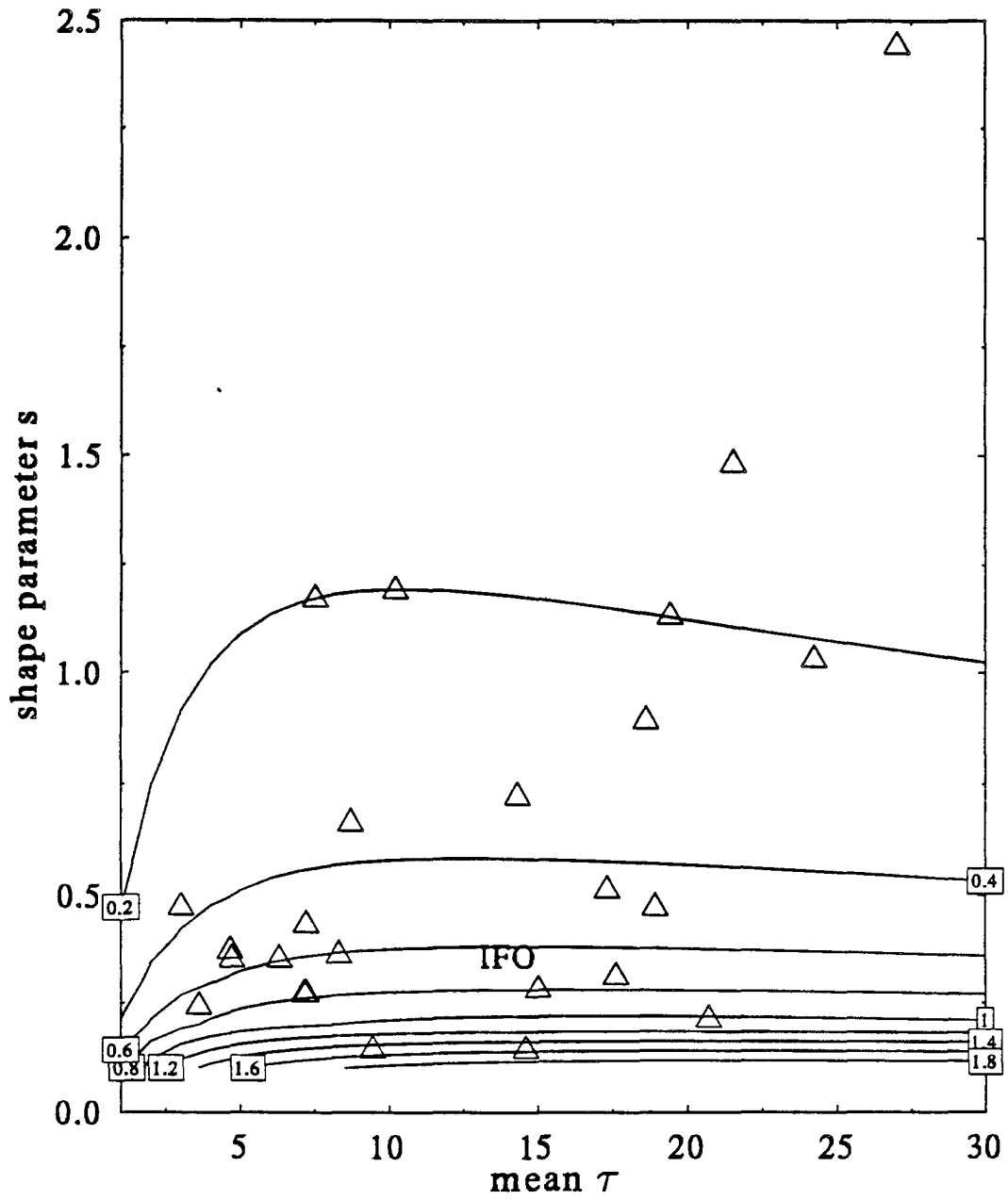
Figure 5.7. Relative reflection error: visible wavelength, low sun

$$\Delta R = \frac{0.3\bar{\tau}}{3.0+\bar{\tau}} \frac{1}{s} . \tag{5.10}$$

The parameterization for the relative error is shown in figure 5.8.

5.2.2 Derivation of a Reduced Optical Thickness

The basis for a reduced optical thickness parameterization is the assumption that there is a value of optical thickness $\tilde{\tau}$ such that

$$\bar{R} = \frac{\gamma\tilde{\tau}}{1+\gamma\tilde{\tau}} . \tag{5.11}$$

The right hand side of equation 5.10 is a common approximation to the full two stream reflection function (Meador and Weaver, 1980; King and Harshvardhan, 1986) and is an excellent approximation for conservative scattering and moderate solar zenith angles. Likewise we approximate the reflection of the mean optical thickness,

$$R(\bar{\tau}) = \frac{\gamma\bar{\tau}}{1+\gamma\bar{\tau}} . \tag{5.12}$$

The parameter γ is constant, being a function only of the single scattering properties of the media, which are not varied. Substituting the previous results into equation 5.11 and solving for $\tilde{\tau}$ yields

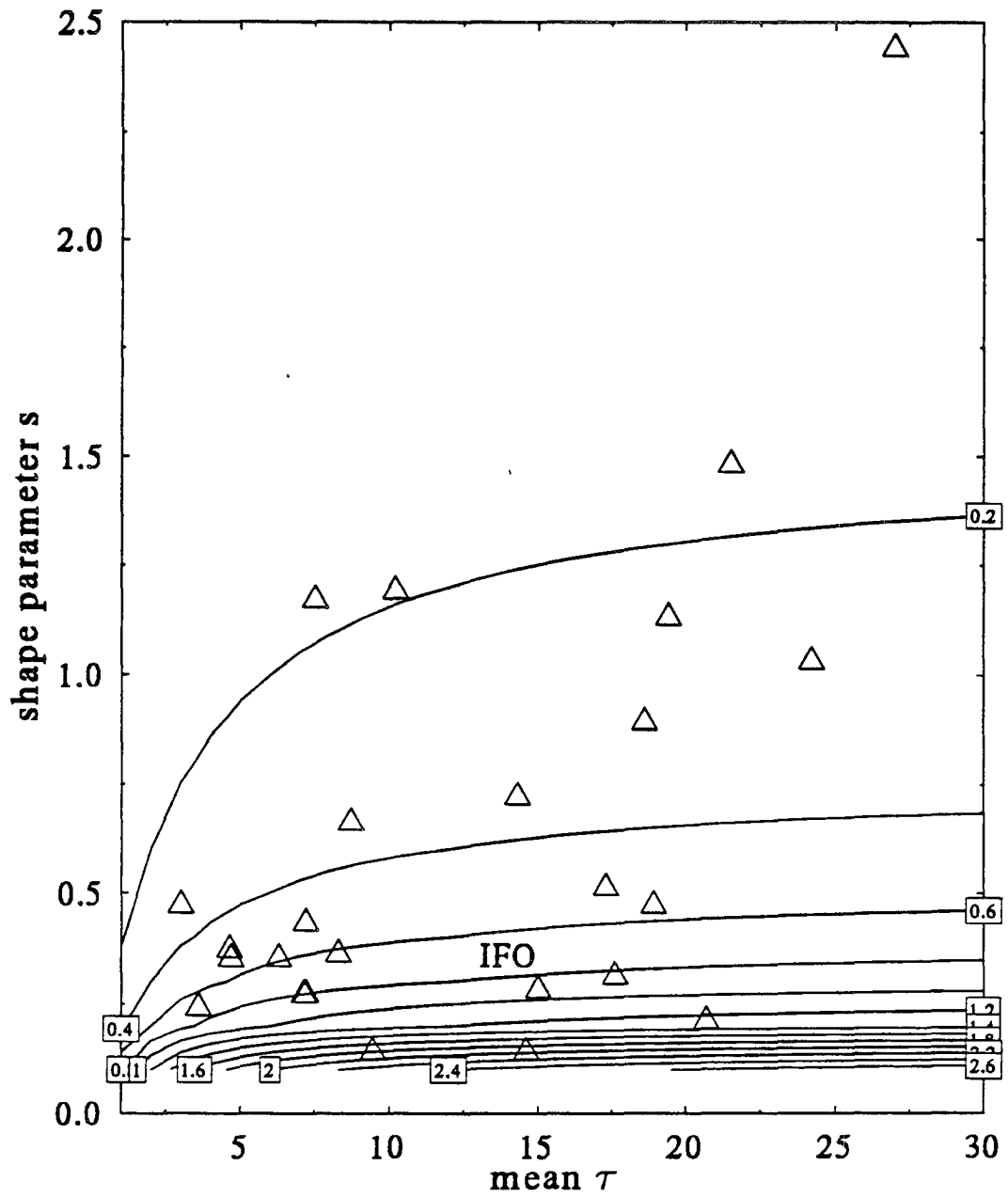$$\tilde{\tau} = \chi(s,\bar{\tau})\bar{\tau} , \tag{5.13}$$

Figure 5.8. Parameterization of the relative error

where

$$\chi(s,\tilde{\tau}) = \frac{s}{s+(1+\gamma\tilde{\tau})\frac{0.3\tilde{\tau}}{3.0+\tilde{\tau}}} \cdot \qquad (5.14)$$

The research of Cahalan *et al* (1994) into the albedo of fractal stratocumulus clouds also lead to an optical thickness reduction factor which is a function of fractal parameters. Davis *et al* (1990) found a power relationship for an effective optical thickness where

$$\tilde{\tau} = \bar{\tau}^{\delta} . \qquad (5.15)$$

5.2.5 Parameterization Compared to IPA Mean Reflection

As in section 5.1.5, contour plots are made of the absolute error between the parameterized mean reflectance and the independent pixel approximation mean reflectance,

$$\delta\tilde{R} \equiv R(\tilde{\tau}) - \bar{R} . \qquad (5.16)$$

Figures 5.9a-d are for visible and ASTEX mean solar, visible and zenith sun, near-infrared and ASTEX mean solar and near-infrared and zenith sun respectively. The largest error typical of any ASTEX day in figure 5.9a is -0.016 and is about -0.003 for the entire IFO. The errors are somewhat larger for the cases of zenith sun because of the error of approximate reflection functions used to derive the reduced optical thickness. Still, the errors are mainly smaller than 5 percent. Likewise in figures 5.9c-d it appears
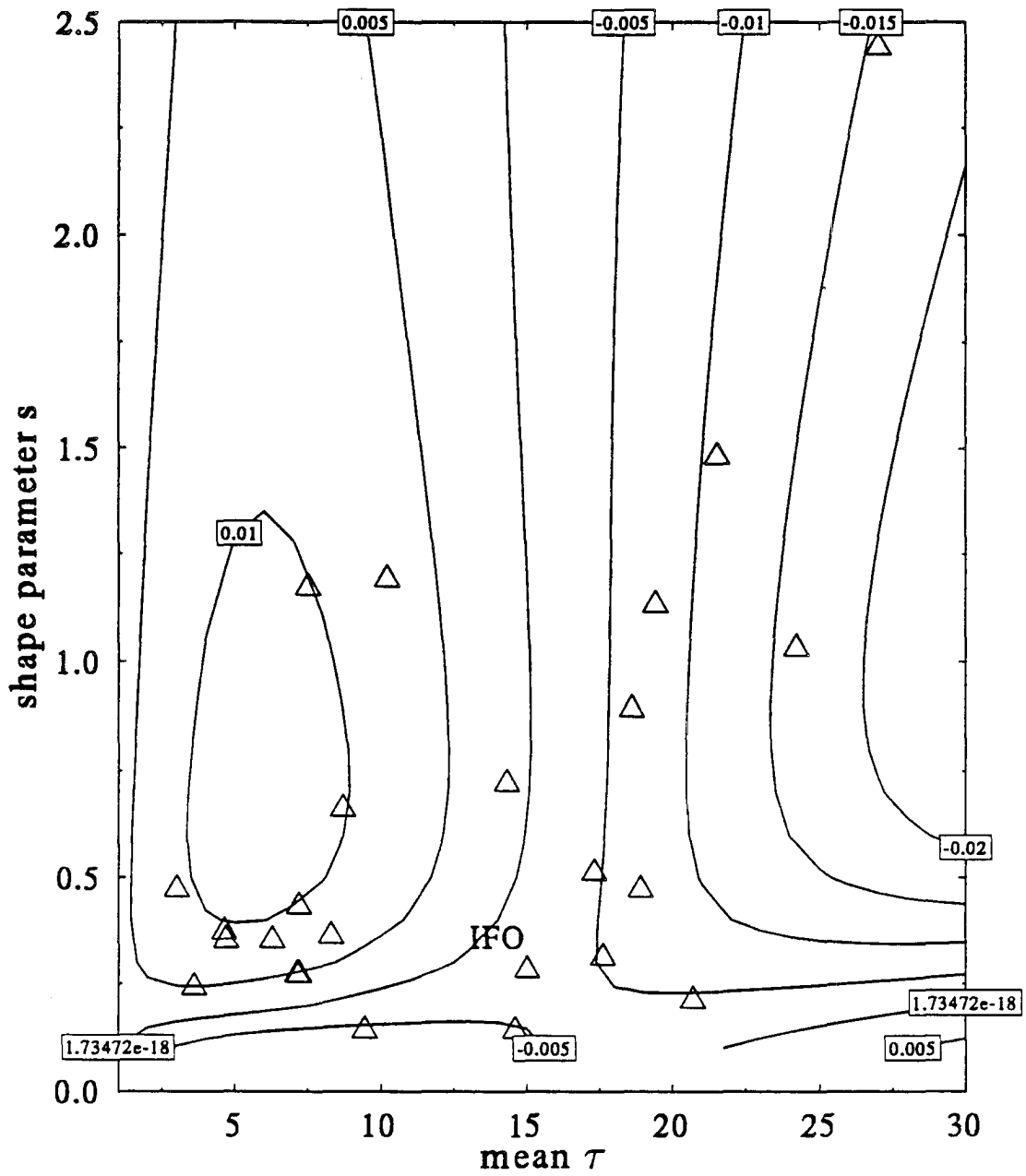
71

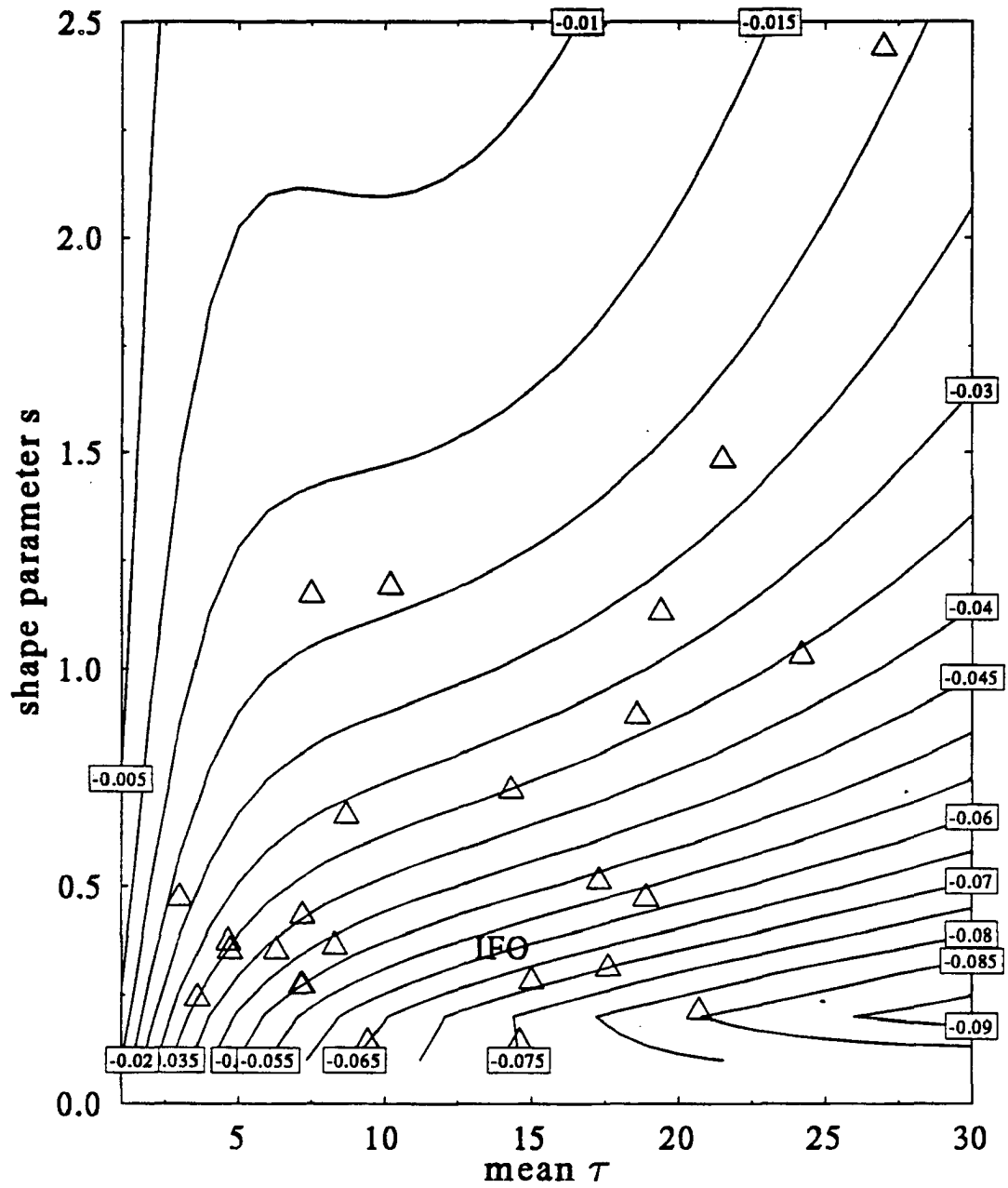Figure 5.9a. Parameterization reflection error: visible wavelength, low sun

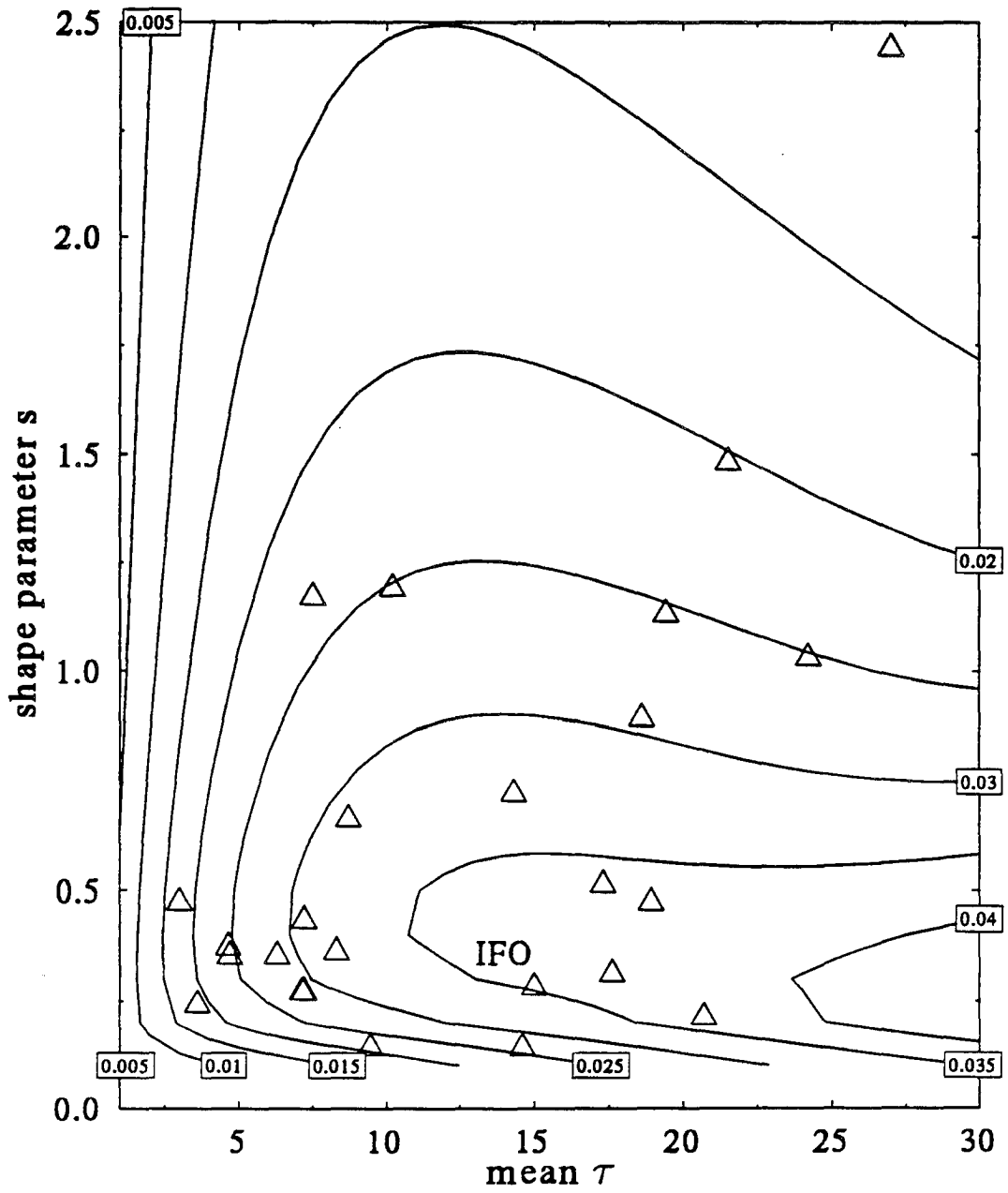Figure 5.9b. Parameterized reflection error: visible wavelength, zenith sun

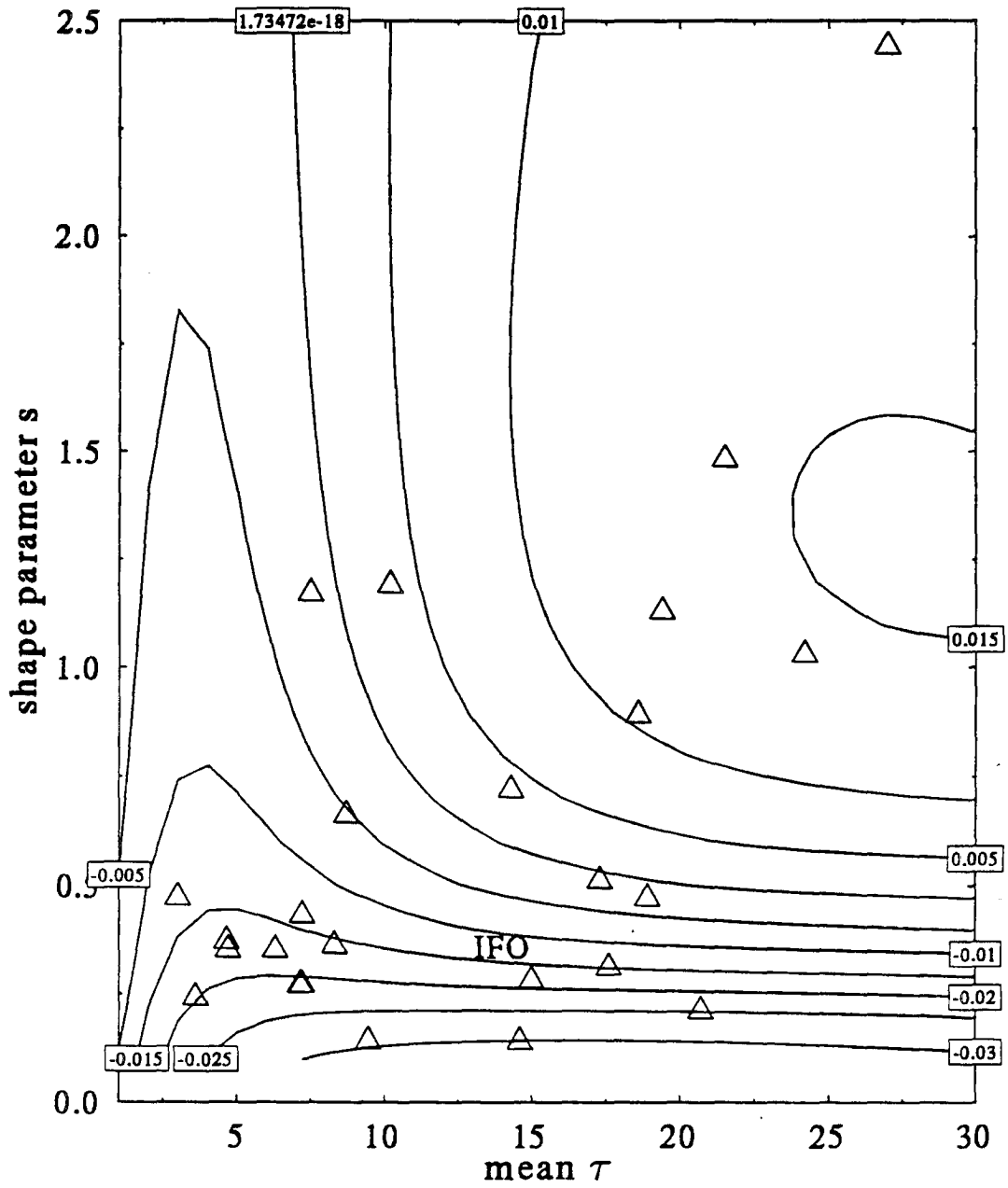Figure 5.9c. Parameterization reflection error: near-infrared wavelength, low sun

Figure 5.9d. Parameterization reflection error: near-infrared wavelength, zenith sun

that the reduced optical thickness parameterization can bring the approximate mean reflection to within 5 percent of the IPA "true" reflectance.

5.2.6 Transmission

Figures 5.10a-d are of transmission errors complementary to the scenarios presented above. As the reduced optical thickness parameterization has been derived from manipulations of a reflection function, one might expect that it would produce somewhat less satisfactory results when used to estimate the mean transmittance of a cloudy domain. This is true, although typical errors are mostly within 0.02 of the IPA truth in 5.10a and 0.05 in c. In the zenith sun scenarios, errors in transmission remain as high as 0.1 but are still much smaller than the errors of figures 5.6.

5.2.7 Summary

The effect of the reduced optical thickness is summarized in table 5.1.

Table 5.1   Absolute error between parameterized and IPA mean optical properties. Computed at the IFO average solar zenith angle and with a gamma pdf fit to the entire IFO LWP distribution.

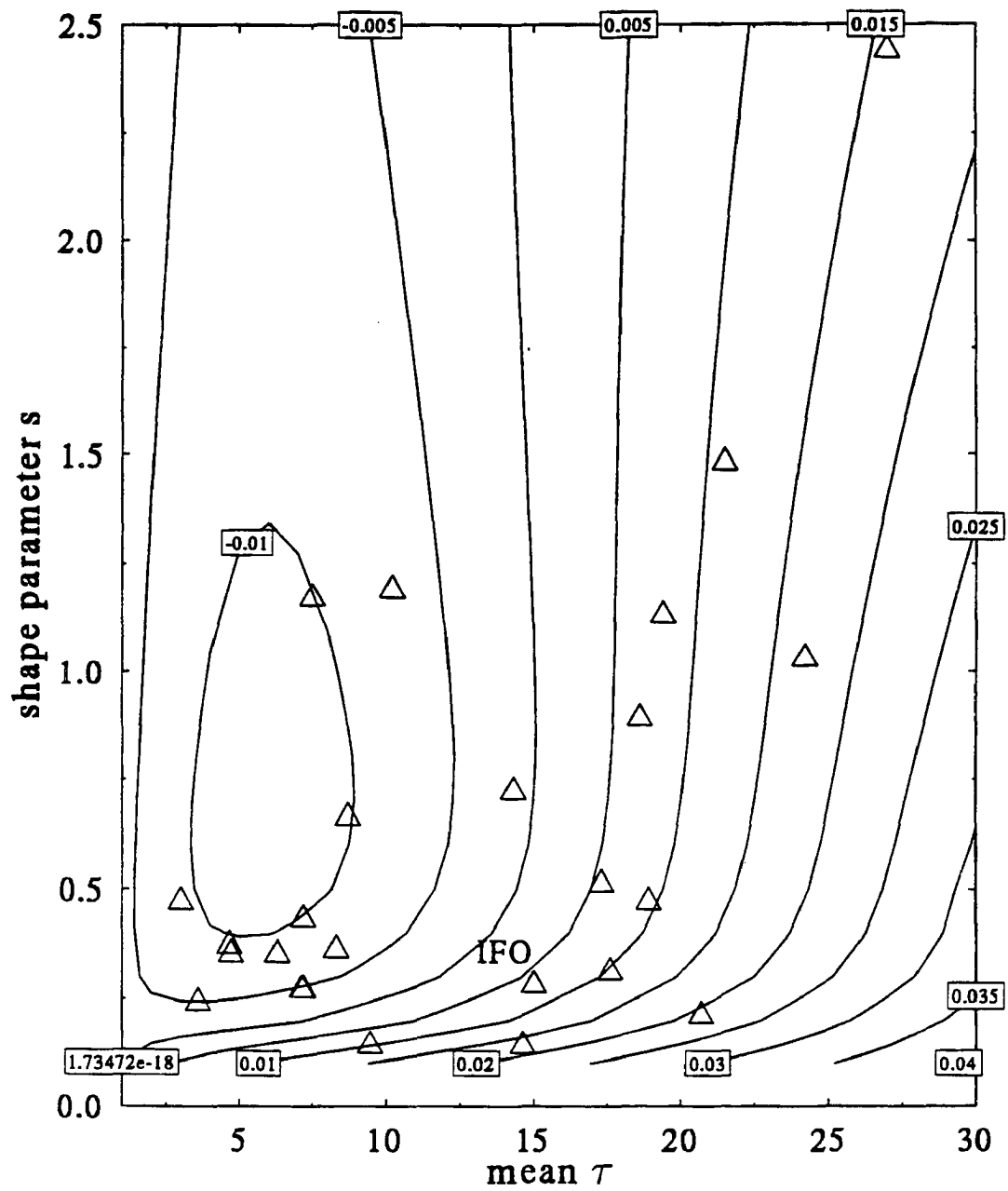| Band	δR	δT
Visible	-0.003	+0.007
Near-Infrared	+0.035	+0.026

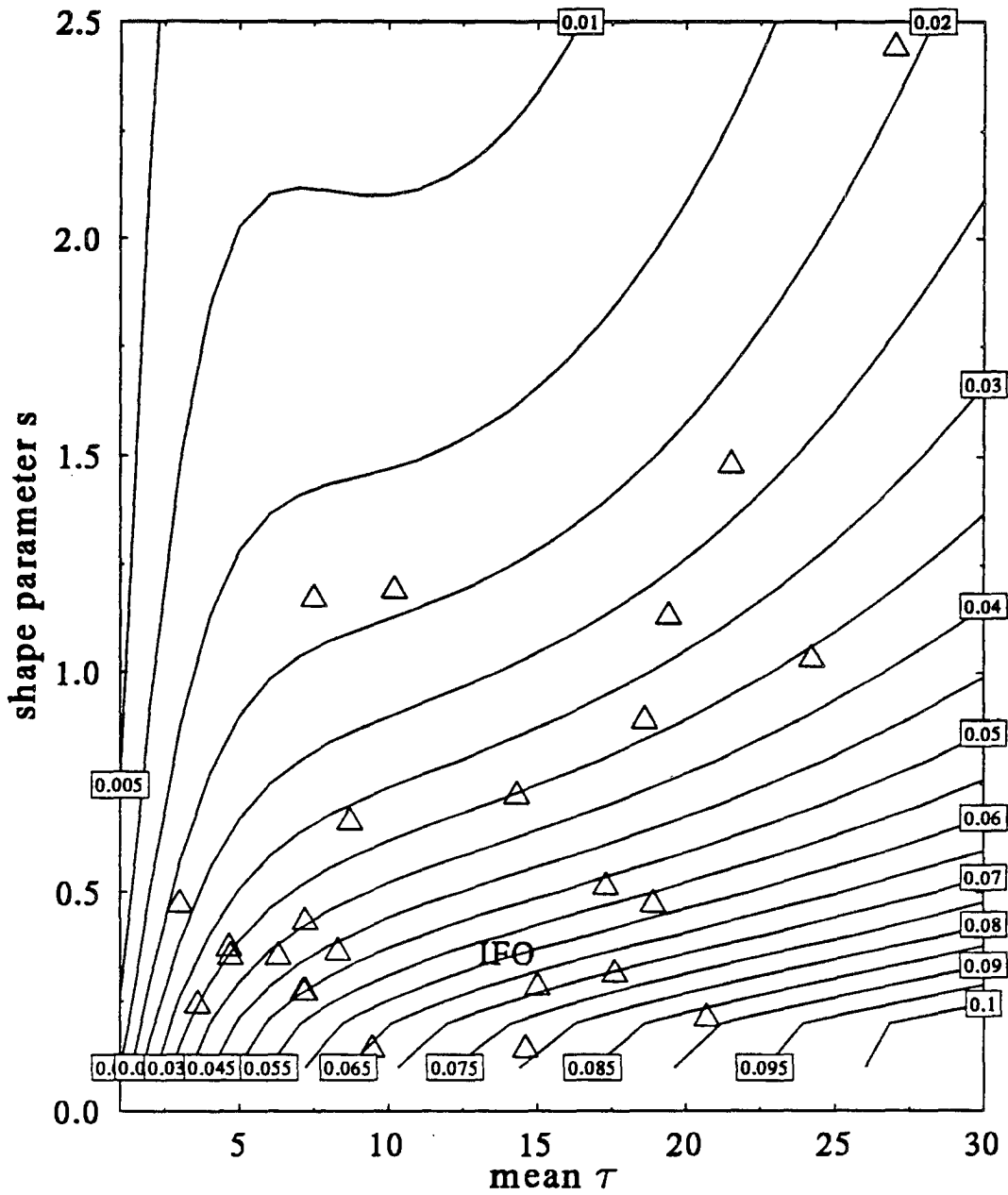Figure 5.10a. Parametrization transmission error: visible wavelength, low sun

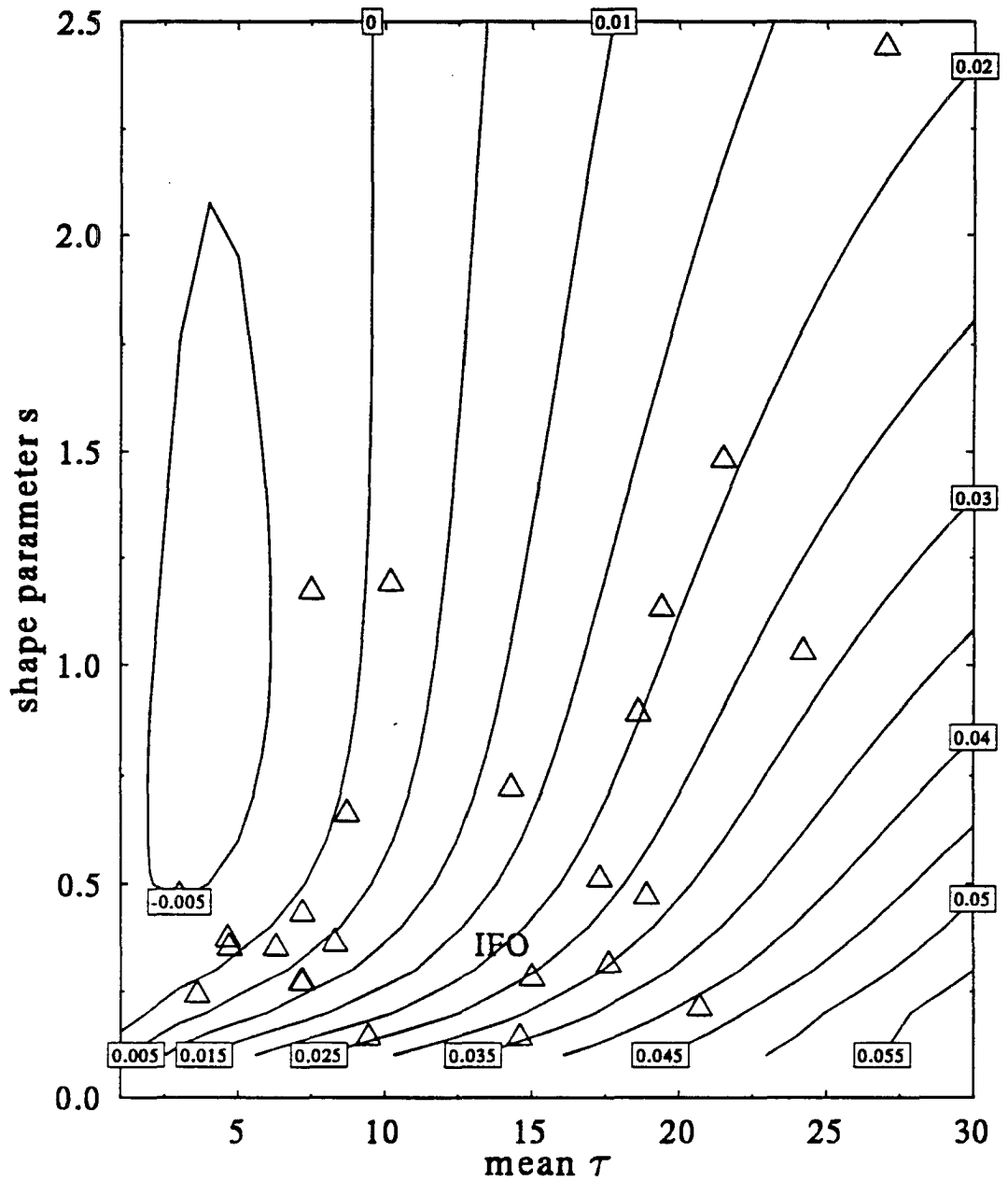Figure 5.10b. Parameterization transmission error: visible wavelength, zenith sun

Figure 5.10c. Parameterization transmission error: near-infrared wavelength, low sun
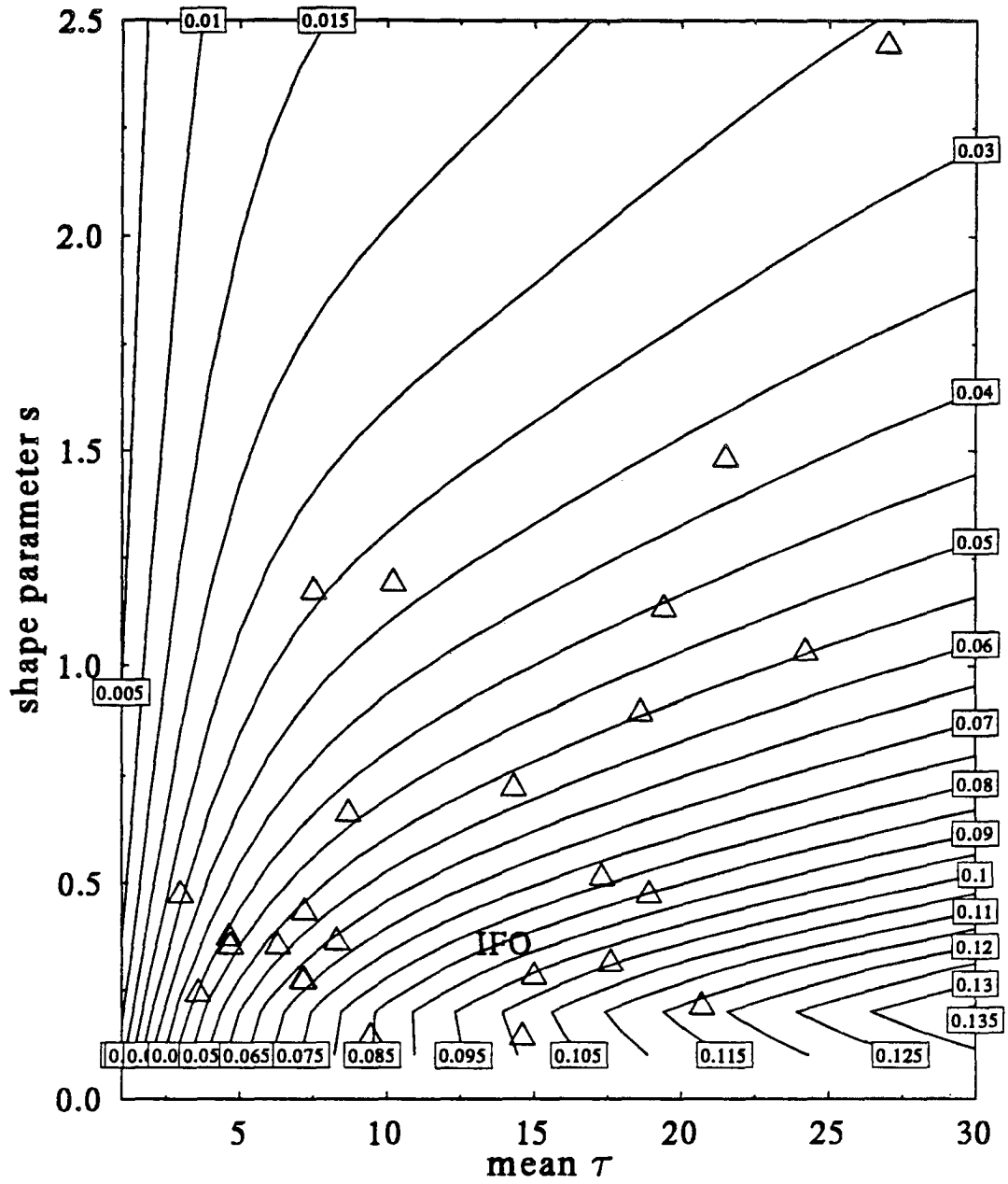
Figure 5.10d. Parameterization transmission error: near-infrared wavelength, zenith sun

Chapter 6. Validation of the Parameterization

6.1 Application to the Estimate of Mean Solar Irradiances

6.1.1 Introduction

The parameterization detailed in the previous chapter may be applied to two classes of radiative transfer problems. The first is for spatially averaged instantaneous transfer of radiation through a horizontally varying optical field; it was in this framework that the calculations of the previous chapters were made. The second application is to the temporally averaged transfer of solar radiation. The data gathered by CSU and NOAA WPL during the ASTEX IFO will only allow comparison to the second kind of application of the reduced optical thickness parameterization. The radiative transfer problems posed within GCMs involve both spatial and temporal averaging.

There are several important assumptions made for the application. One is that the distribution of vertically integrated liquid water is isotropic. That is to say that the LWP measured in time by the WPL microwave radiometer is representative of the spatial distribution of the same quantity over a much larger area. There is no quantitative measure of the validity of this assumption. Since the LWP is measured from a zenith pointing instrument and the sun never actually reaches true zenith, there is no guarantee

that the cloudiness measured is the same as that which interacts with the solar beam. Lappen (1994) showed that topographical effects exist in the flow over the island of Porto Santo and these effects may include a downstream bias in cloudiness. The mean wind direction measured at the IFO site was 8° West of North and the most probable direction was 35° West of North. If there is a positive downstream bias in cloudiness it would have an impact on the solar irradiance measured at the IFO site since the sun is always in the southerly and downstream sky relative to the instruments.

The second assumption made is that solar irradiance is a linear function of the cosine of the solar zenith angle. To evaluate this assumption, linear regressions have been performed upon the diurnally averaged clear sky and all sky data sets. The results are tabulated below in table 6.1.

Table 6.1 Linear Regression of the dependence of surface solar irradiance on cosine of the solar zenith angle.

Data	Constant (W m^{-2})	Coefficient (W m^{-2} μ_0^{-1})	R^2
Clear Sky	-87.6	1151.6	0.99613
All Sky	-62.9	828.8	0.9607

The mean solar irradiance from the clear sky reference data is 361 W m^{-2} and the irradiance, using the regression, at the day's average elevation of $\mu_0 = 0.612$ is 360 W m^{-2}. When the entire diurnally averaged data set including clear and cloudy skies is considered, one finds that the daily mean is 257 W m^{-2}. The irradiance modeled by linear regression is 259 W m^{-2} at the mean solar zenith angle ($\mu_0 = 0.612$). The dependence of the

diurnally averaged surface solar irradiance upon μ_0 is shown in figure 6.1. As there is more cloud cover in the morning hours than in the afternoon, the points fall into two clusters. The relationship in this case is quite linear up to $\mu_0 = 0.85$ but at higher zenith angles this state breaks down. The nearly linear relationship between the surface solar irradiance and the cosine of the solar zenith angle will allow the daily average irradiance to be estimated from a single calculation and the confidence in this estimate will be comparable to the confidence in the isotropy of the cloud cover.

6.2 A Model of Daily Averaged Irradiance

6.2.1 The Model

For the purpose of illustrating the use of the variance-reduced optical thickness parameterization a simple model of solar radiative transfer has been formulated. The solar spectrum is resolved as two broad bands which correspond to the visible and near-infrared pyranometer measurements. The visible (0.3-0.7 μm) and near-infrared (0.7-2.8 μm) bands are assumed to contain equal amounts of power at the top of the atmosphere. The model atmosphere is considered to be of two homogeneous layers, a tropospheric layer and a boundary layer. Since we are considering clouds which top the marine boundary layer, cloudiness occupies the bottom layer of the model. The top layer of the model which comprises most of the actual depth of the atmosphere contains the other important components of the radiative transfer problem, rayleigh scattering and water vapor absorption. For simplicity's sake, all rayleigh scattering is assumed to occur in the visible band, and all absorption by water vapor occurs in the near-infrared band. A schematic illustration of the model, without cloudiness, is shown in table 6.2.
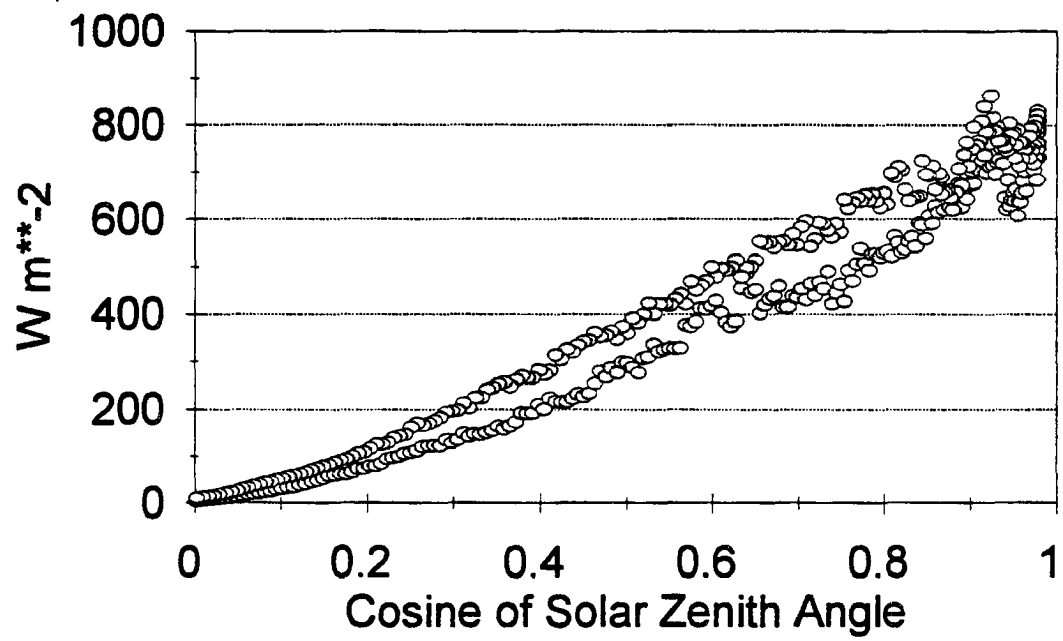
Figure 6.1. Cosine dependence of irradiance

Table 6.2 Optical components of the model clear sky

	Visible	Near-Infrared
Tropospheric Layer	Rayleigh Scattering: $g = 0$, $\varpi_0 = 1$, $\tau = 0.4$	Water Vapor: $g = 0$, $\varpi_0 = 0$, $\tau = 0.12$
Boundary Layer	Haze: $g = 0.75$, $\varpi_0 = 0.99$, $\tau = 0.13$	Linear Combination of H_2O ($\tau_v = 0.3$) and Haze: $g = 0.75$, $\varpi_0 = 0.8$, $\tau = 0.16$

The optical thickness of boundary layer aerosol is adopted from Pinker and Laszlo (1992). The optical thickness of the Rayleigh scattering layer is determined from an iterative procedure which selects the value which produces the best fit to the observed cloudless sky diffuse irradiance. Likewise, the total optical thickness of water vapor absorption is determined to be that which produces the best fit to the estimate, in chapter 3, of cloudless sky H_2O absorption in the 0.7-4 μm band. When multiple components are present, as in the near-infrared boundary layer box of table 6.2, the optical parameters are combined linearly. Cloud completely replaces the haze, when present. The asymmetry parameter for cloud droplet scattering is fixed at 0.85 and the single scattering albedo is 1 for visible radiation and 0.995 for near-infrared radiation. The optical thickness of cloud is parameterized in terms of vertically integrated liquid water in units of g m^{-2} and droplet effective radius in units of μm, $\tau = 3W/2r_e$ (Stephens, 1978). It is assumed for the following calculations that the effective radius is always 10 μm, and scattering is modeled with a single Henyey-Greenstein phase function. Reflection and transmission functions

of the layers are calculated independently and are subsequently combined by the adding method to obtain an integrated reflectance and transmittance.

The surface solar irradiance is calculated as a sum of appropriately weighted clear and cloudy sky components,

$$\bar{F}(\bar{\theta}_0) = C'(\bar{\theta}_0)F_{cld}(\bar{\theta}_0) + (1 - C'(\bar{\theta}_0))F_{clr}(\bar{\theta}_0) , \qquad (6.1)$$

where the effective cloud fraction C' is related to the horizontally projected cloud fraction C by a parameterization adapted from that of Davis, *et al* (1979),

$$C'(\theta_0) = \text{MAX}[(1 + C_{cu}\tan\theta_0)C, 1] . \qquad (6.2)$$

where C_{cu} is the fractional amount of cumulus clouds. When there are no cumulus clouds, cloud sides are not an important consideration and the effective cloud cover will be identical to the horizontal cloud cover. The value of C_{cu} that is used is 0.33 (see tables 2.1 and 2.2). Equation 6.2 yields, for the daily average solar zenith angle of 52.3 degrees and the PRT6 derived cloud cover of 53 percent, an effective cloud amount of 0.76. This is remarkably close to the effective cloud amount of 0.75 that was deduced from the CRF of direct irradiance in section 3.4.3.

The flux weighting scheme is depicted schematically in figures 6.2a-c. Figure 6.2a shows an inhomogeneus cloud field illuminated by the sun at a relatively low angle and the difference between the horizontal cloud fraction and the effective cloud fraction. Figure 6.2b shows the conventional parameterization for surface irradiance in such a regime, a sum of clear and overcast fractions weighted by the horizontal cloud cover.
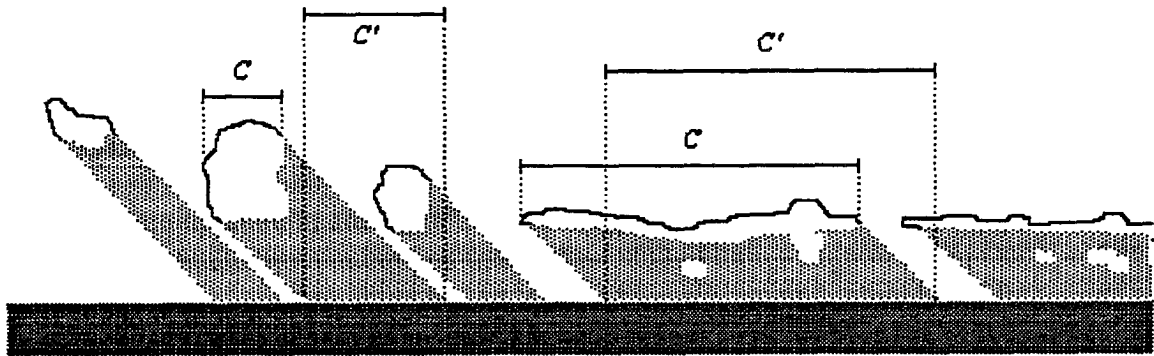
Figure 6.2a An inhomogeneous field of clouds and the associated horizontal cloud fraction C and effective cloud fraction C'

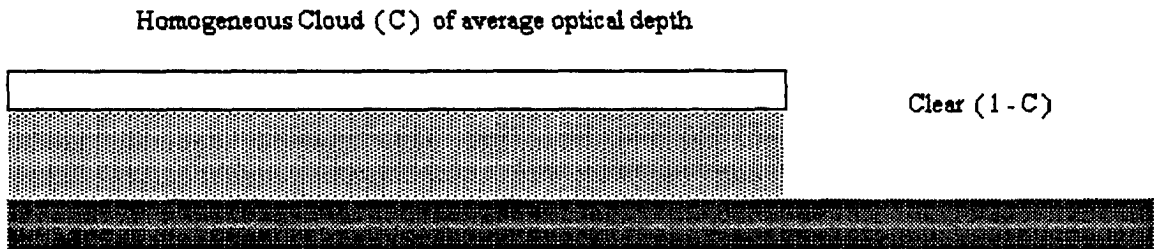Homogeneous Cloud (C) of average optical depth

Clear (1 - C)

Figure 6.2b Conventional approximation to the problem posed in figure 6.5a, the domain is divided into a clear fraction and a fraction inhabited by homogeneous cloud with mean properties. The horizontal cloud fraction is used to weight the clear and cloudy fluxes.

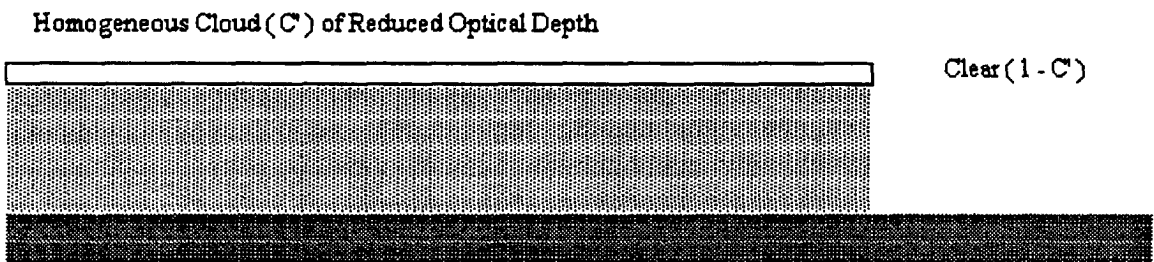Homogeneous Cloud (C') of Reduced Optical Depth

Clear (1 - C')

Figure 6.2c New parameterization which an effective cloud fraction C' which accounts for finite geometry and a reduced optical thickness which better represents the radiative interaction of a horizontally variable cloud layer.

This scheme will overestimate the surface irradiance in the unclouded region because the cloud fraction is anomalously low and will underestimate the irradiance under the clouded region because the optical thickness is too large. Figure 6.2c shows the parameterization developed in the course of this research. An effective cloud amount is used to properly account for the effect of a cloud's vertical extent on the direct surface irradiance and a reduced optical thickness is implemented in the cloud region to account for the cloud inhomogeneity.

6.2.2 Surface Irradiance Under Cloudless Sky

When the model calculations are executed for the cloudless sky case (parameters as in table 6.2) with the sun at its daylight mean position of $\mu_0 = 0.612$, one obtains a visible surface irradiance (normalized to a diurnal average) of 176 W m^{-2} and a near-infrared irradiance of 182 W m^{-2}. This is very close to the observed cloudless irradiances (table cc) which are 178 W m^{-2} in the visible and 183 W m^{-2} in the near-infrared.

6.2.3 Surface Irradiance under Overcast Conditions

Figure 6.3 shows the surface solar irradiance in each broad band as a function of the optical thickness of cloud in the boundary layer of the two layer model. Although a two layer radiative transfer model is inadequate for many applications it is probably sufficient for estimates of surface irradiance, at least in a narrow band. The major simplification of this model, and the one that has the most potential for error, is the crude spectral resolution. The Pinker and Laszlo surface solar irradiance algorithm (1992), considers four visible bands rather than the one here, mostly to resolve ozone absorption which is neglected in the present model. Optical properties of cloud droplets are rather
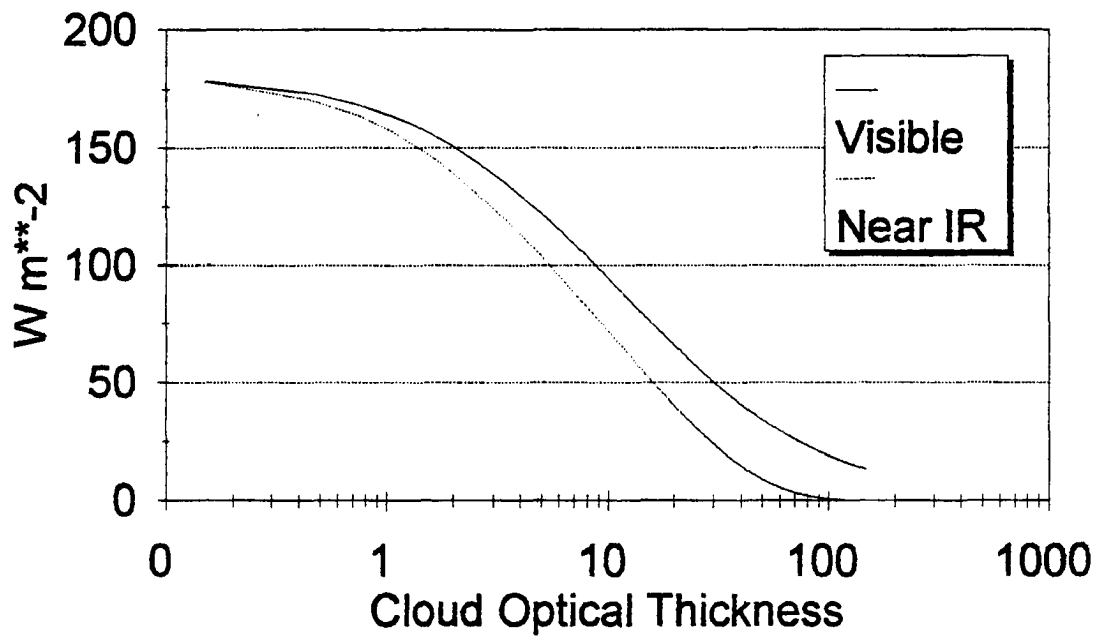
Figure 6.3. Surface solar irradiance as a function of cloud optical thickness.

constant within the visible range but vary significantly within the near-infrared range. More accuracy could be gained, theoretically, by increasing the spectral and vertical resolution of the present model, but it is sufficient for the purpose of illustrating the utility of the parameterizations developed in the preceding chapters.

6.3 Simulating Daily Average Irradiance

6.3.1 Simulation with Mean Optical Thickness

The character of cloudiness over the IFO period is illustrated in figure 5.3. The data are all daylight (6 to 20 GMT) times in the 1-28 June period. The mean vertical liquid water path when cloud was present was 100 g m^{-2} and therefore the mean optical thickness was, by the parameterization mentioned above, $\bar{\tau} = 15$. Introduction of this monthly mean cloudiness into the boundary layer of the two band model along with use of the horizontal cloud fraction parameterization (parameterization I) yields a result of 238 W m^{-2} surface solar irradiance at the mean solar angle $\theta_0 = 52$ degrees. This is much less than the observed monthly mean of 257 W m^{-2}. Evidently, knowledge of the monthly daylight mean optical thickness and the horizontal cloud fraction are not sufficient for accurate determination of the monthly mean surface irradiance. Use of the effective cloud fraction and mean optical thickness (parameterization II) results in less agreement with observation, 186 W m^{-2}. Parameterization I can yield irradiances within 20 W m^{-2} of the observation because the anomalous clear sky irradiance offsets the anomalously dark overcast region.

6.3.2 Independent Pixel Approximation

Using the histogram of LWP observed during all daylight periods of the IFO (figure 5.3) one can use the independent pixel approximation of radiative transfer to estimate the surface solar irradiance. Using the same two layer and two band model and summing over the contributions for every interval of LWP, a mean irradiance of 248 W m^{-2} was obtained. This is somewhat smaller than the observed average, consistent with our expectation of the IPA to underestimate the mean transmission.

6.3.3 Reduced Optical Thickness

If the LWP data are fit to a gamma distribution with the same mean and variance, we obtain a shape parameter of 0.29 for the cloudy fraction of the sky. The reduction factor corresponding to this distribution, as defined in equation 5.14, is 0.304. When cloud of a reduced optical thickness $\tilde{\tau} = 4.57$ and a horizontal coverage of 53 percent (parameterization III) is placed into the model, a surface solar irradiance of 292 W m^{-2} is obtained. The final parameterization, reduced optical thickness and an increased effective cloud fraction, produces the result most near to the observation, 264 W m^{-2}. The reduced optical thickness parameterization is capable of yielding a surface irradiance within 10 W m^{-2} of observation.

The following tables summarize the cloud forcing during the ASTEX/FIRE II IFO. All values are averages over the period of 0600-2000 GMT which are further normalized to the length of day.

Table 6.1 Deviations from Irradiance Measured under Cloudless Conditions (CSD)

Observed	-104 W m^{-2}
Independent Pixel Approximation	-113 W m^{-2}
Parameterization I ($\bar{\tau}$, C)	-123 W m^{-2}
Parameterization II ($\bar{\tau}$, C')	-175 W m^{-2}
Parameterization III ($\tilde{\tau}$, C)	-69 W m^{-2}
Parameterization IV ($\tilde{\tau}$, C')	-97 W m^{-2}

6.3.4 Further Validation

As a further test of the reduced optical thickness parameterization, estimates of the mean surface solar irradiance for each day of the IFO period have been made using the same radiative transfer code and a similar method of matching a gamma distribution to the LWP data observed during the particular day. The observed irradiances and those modeled using mean and reduced optical thicknesses (parameterizations I and IV) are shown in figure 6.4. The model does not perform as well for individual days as it did for the entire IFO period because of the breakdown of the fundamental assumptions. The distribution of LWP within a 24 hour period is less isotropic and the linearity assumption is also invalid. The solar irradiance as a function of the solar zenith angle is shown for two days of the IFO, June 15 and 16 (figures 6.4 and 6.5). The R^2 of a linear fit to these curves are 0.533 and 0.802 respectively, much less than for the IFO diurnal average. Still, from these calculations it can be concluded that the reduced optical thickness parameterization is a substantial improvement over the use of a mean optical thickness. Use of the mean yields results within 10 W m^{-2} of the IFO values on nine days. Use of
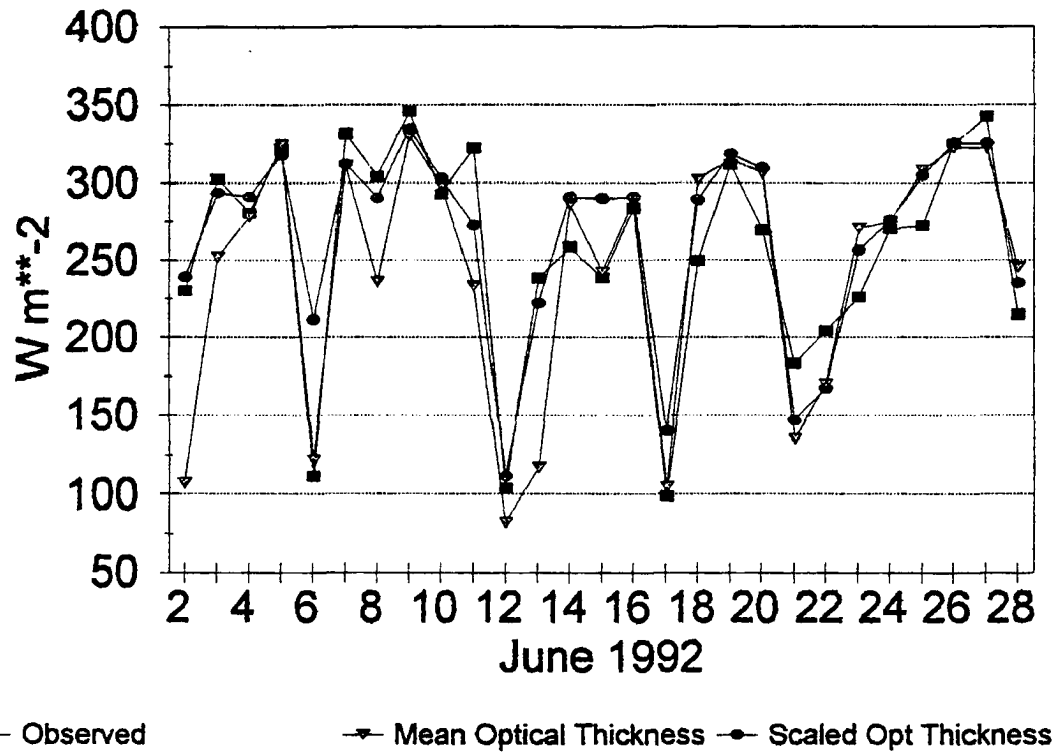
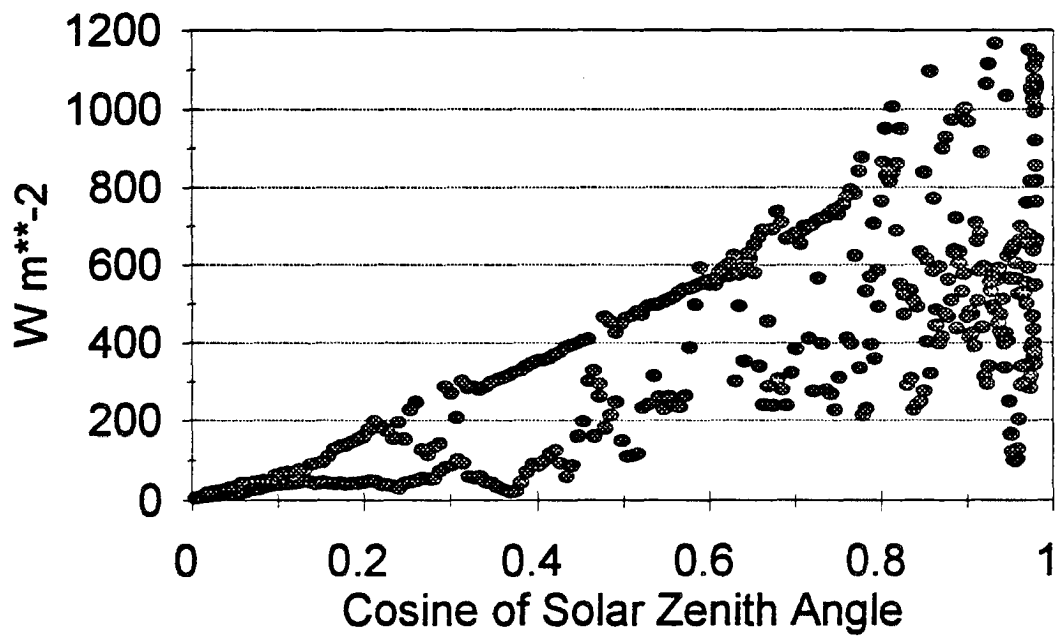Figure 6.4. Observed and modeled surface solar irradiance

93

Figure 6.5. Solar Irradiance, June 15

Figure 6.6. Solar Irradiance, June 16
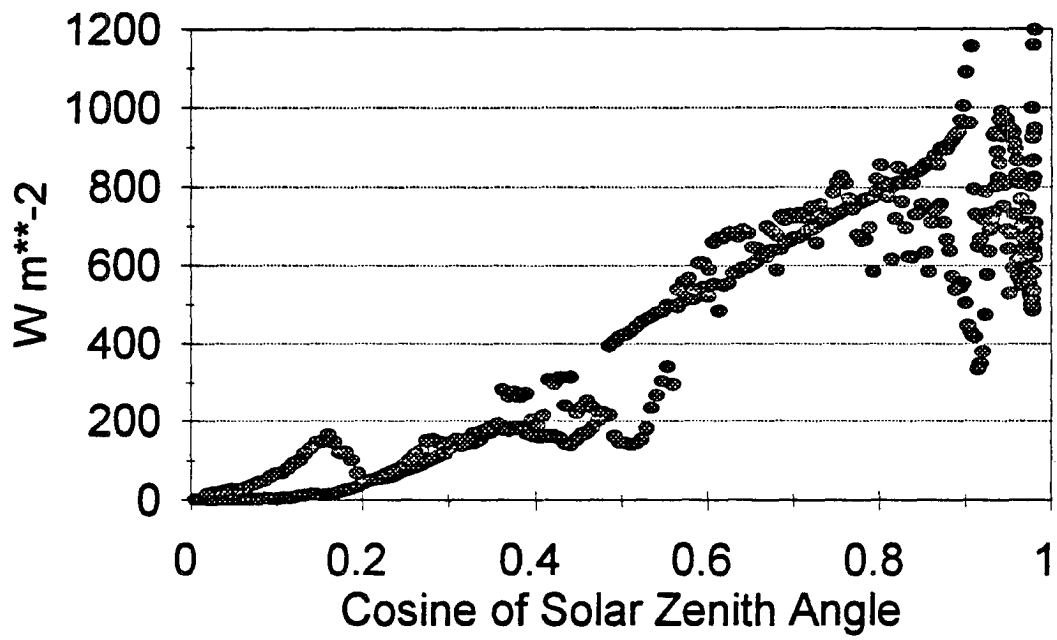
educed thickness parameterization is more effective, producing results within 10 W m^{-2} on ten of the IFO days. Considering the complications inherent in matching local irradiance measurements to radiative transfer calculations, these tests validate the reduced optical thickness parameterization for the marine stratocumulus cloud regime characteristic of the ASTEX campaign.

Chapter 7. Conclusions

7.1 Cloud Cover

Cloud cover observed at Porto Santo during the ASTEX IFO was similar to climatological values for the summer months. The IFO mean cloud cover derived from the ceilometer was 48 percent, and 53 percent was derived from the PRT-6 bolometer. The average diurnal cycle of cloudiness exhibited a minimum of 30 percent and a maximum of 70 percent. Observations also showed a mid-morning peak of cloudiness, consistent with findings of other authors. A histogram of cloud cover occurrence demonstrates that most cloud cover is due to the intermittent occurrence of overcast conditions.

7.2 Surface Solar Irradiance

There was a sufficient occurrence of clear sky conditions during the IFO to allow for the construction of a complete diurnal clear sky surface irradiance data set which includes visible and near-infrared and direct and diffuse components. This has allowed the cloud radiative forcing upon any single measurement to be determined. The average CRF of the net surface irradiance during the IFO period was -102 W m^{-2}. The direct CRF was -174 W m^{-2} and the diffuse CRF was +73 W m^{-2}. The fact that average CRF is a

sum of a negative term due to shadowing of direct irradiance and a positive term due to the radiation a cloud scatters down to the surface is not widely acknowledged. Measurements of irradiance were identified as occurring under either stratus/stratocumulus or cumulus regimes and the daily average CRF of each of these regimes was estimated to be -131 W m^{-2} and -66 W m^{-2} respectively.

7.3 Parameterization

The conventional parameterization for fluxes on the boundary of an inhomogeneous cloud layer is to compute the flux from a plane-parallel cloud of optical thickness equal to the average optical thickness of the broken cloud and then to weight this flux with an effective cloud amount which is the ratio of the true mean flux to the plane-parallel flux. This is a circular parameterization and is based on an assumption that flux differences are mostly dependent upon cloud amount. A new parameterization which implements a larger effective cloud cover and a smaller effective optical thickness has been shown to be an improvement over the conventional parameterization. The effective optical thickness is the product of the mean optical thickness and a reduction factor. The reduction factor, shown in equation 5.14, is very sensitive to the variance of optical thickness and less sensitive to variation in the mean optical depth of a cloudy region.

The reduced optical thickness parameterization has been developed within the constraints of several assumptions. The independent pixel approximation has been used, which is equivalent to the assumption that the actual spatial structure of a cloud is less important to irradiance calculations than the statistical variation of it's optical properties. It has also been assumed that one-dimensional radiative transfer methods can be used to

address the problem of irradiances connected to variable cloud domains. This is a common assumption and one that is improved in this case as averaging over an ensemble of independent pixel calculations will reduce the net leakage errors. Many simulations using multi-dimensional radiative transfer methods are yet needed before the validity of these assumptions can be truly known under a wide range of cloud properties and geometries.

Literature Cited

Albrecht, B. A., 1981: Parameterization of trade-cumulus cloud amounts. *J. Atmos. Sci.*, 38, 97-105.

Briegleb, B. P., P. Minnis, V. Ramanathan, and E. Harrison, 1986: Comparison of Regional Clear-Sky Albedos Inferred from Satellite Observations and Model Calculations. *J. Climate Appl. Meteor.*, 25, 214-226.

Cahalan, R. F., 1989: Overview of Fractal Clouds. *Advances in Remote Sensing Retreival Methods*, A. Deepak, ed., 371-388.

Cahalan, R. F., W. Ridgway, W. J. Wiscombe, and T. L. Bell, 1994: The Albedo of Fractal Stratocumulus Clouds. *J. Atmos. Sci.*, 51, 2434-2455.

Chandresekhar, S., 1960: *Radiative Transfer.* 2nd ed. Dover.

Cotton, W. R., and R. A. Anthes, 1989: *Storm and Cloud Dynamics.* Academic Press.

Cox, S. K., C. Cornwall, W. Cotton, J. Davis, J. Kleist, T. McKee, Q. Shao, D. Randall, W. Schubert, D. Wood, S. Frisch, M. Hardesty, R. Kropfli, J. Snider, and P. Anikin, 1993a: CSU/NOAA-WPL FIRE II-ASTEX Field Experiment: Description of Field Deployment Phase. Colorado State University Department of Atmospheric Science Paper No. 523.

Cox, S. K., S. Gillies, A. Heidinger, and C. Keith, 1993b: CSU ASTEX Surface Data Sets from Porto Santo (June 1-28, 1992). FIRE Series No. 9. Colorado State

University Department of Atmospheric Science Paper No. 530.

Davis, J. M., S. K. Cox, and T. B. McKee, 1979: Vertical and Horizontal Distribution of Solar Absorption in Finite Clouds. *J. Atmos. Sci.*, 36, 1976-1984.

Davis, A., P. Gabriel, S. Lovejoy, D. Schertzer, and G. L. Austin, 1990: Discrete Angle Radiative Transfer. 3. Numerical Results and Meteorological Applications. *J. Geophys. Res.*, 95, D8, 11729-11742.

Fairall, C. W., J. E. Hare, and J. B. Snider, 1990: An Eight-Month Sample of Marine Stratocumulus Cloud Fraction, Albedo, and Integrated Liquid Water. *J. Climate*, 3, 847- 864.

Garratt, J. R., 1992: *The Atmospheric Boundary Layer*. Cambridge University Press.

Garstang, M., and A. K. Betts, 1974: A review of the tropical boundary layer and cumulus convection: structure, parameterization, and modeling. *Bull. Am. Meteorol. Soc.*, 55, 1195-1205.

Haurwitz, B., 1945: Insolation in relation to cloudiness and cloud density. *J. Meteorol.*, 2, 154-166.

Johnson, D. W., G. M. Martin, J. Taylor, and M. Gibbs, 1992: ASTEX Flight Summary for U.K. C-130, 30th May-24th June 1992. Meteorological Research Flight.

Kelly, M. A., 1994: Investigations of the earth's entropy budget: comparison with a general circulation model. M. S. Thesis, Colorado State University, Department of Atmospheric Science.

King, M. D., and Harshvardhan, 1986: Comparative Accuracy of Selected Multiple Scattering Approximations. *J. Atmos. Sci.*, 43, 784-801.

Lappen, C., 1994: An Assessment of the Extent of the Contamination of Measurements Taken on Porto Santo during ASTEX. M. S. Thesis, Colorado State University, Department of Atmospheric Science.

Levy, R., D. Randall, and W. Schubert, 1993: An Overview of the ASTEX Data Collected at Porto Santo. Colorado State University Department of Atmospheric Science Paper No. 539.

Liou, K., 1992: *Radiation and Cloud Processes in the Atmosphere*. Oxford University Press.

McKee, T. B., and S. K. Cox, 1974: Scattering of Visible Radiation by Finite Clouds. *J. Atmos. Sci.*, 31, 1885-1892.

Meador, W. E., and W. R. Weaver, 1980: Two-Stream Approximations to Radiative Transfer in Planetary Atmospheres: A Unified Description of Existing Methods and a New Improvement. *J. Atmos. Sci.*, 37, 630-643.

Morcrette, J.-J., and Y. Fouquart, 1986: The Overlapping of Cloud Layers in Shortwave Radiation Parameterizations. *J. Atmos. Sci.*, 43, 321-328.

Pinker, R. T., and I. Laszlo, 1991: Model Surface Solar Irradiance for Satellite Applications on a Global Scale. *J. Appl. Meteor.*, 31, 194-211.

Poellet, M. R., and S. K. Cox, 1975: Computer simulation of irradiance measurements from aircraft. Colorado State University Department of Atmospheric Science Paper No. 233.

Press, W. H., B. P. Flannery, S. A. Teukolsky, and W. T. Vetterling, 1992: *Numerical Recipes in C; The Art of Scientific Computing*. 2nd ed. Cambridge University Press.

Randall, D. A., 1984: Stratocumulus Cloud Deepening through Entrainment. *Tellus*, 36A, 446-457.

Rosenberg, N. J., B. L. Blad, and S. B. Verma, 1983: *Microclimate: The Biological Environment*, 2nd ed. John Wiley & Sons, New York.

Stephens, G. L., 1978: Radiation Profiles in Extended Water Clouds. II: Parameterization Schemes. *J. Atmos. Sci.*, 35, 123-2132.

Stephens, G. L., 1988: Radiative Transfer through Arbitrarily Shaped Optical Media. Part II: Group Theory and Simple Closures. *J. Atmos. Sci.*, 41, 725-735.

Stephens, G. L., P. M. Gabriel, and S.-C. Tsay, 1991: Statistical Radiative Transport in One-dimensional Media and its Application to the Terrestrial Atmosphere. *Trans. Theory and Stat. Physics*, 20, 139-175.

Stull, R. B., 1985: A fair-weather cumulus cloud classification scheme for mixed-layer studies. *J. Clim. Appl. Meteorol.*, 24, 49-56.

Thompson, T. M., 1981: Pyrheliometer observations as an indicator of the climatological persistence of clouds. NOAA Tech. Memorandum ERL ARL-97.

Twomey, S., H. Jacobowitz, and H. B. Howell, 1966: Matrix Methods for Multiple-Scattering Problems. *J. Atmos. Sci.*, 23, 289-296.

Warren, S. G., C. J. Hahn, J. London, R. M. Chervin, and R. L. Jenne, 1986: Global Distribution of Total Cloud Cover and Clound Type Amount over Land. NCAR/TN-273+STR, National Center for Atmospheric Research.

Welch, R. M., M. G. Ravichandran, and S. K. Cox, 1986: Prediction of Quasi- Periodic Oscillations in Radiation Fogs. *J. Atmos. Sci.*, 43, 633-651.

Welch, R. M., S. K. Cox, and J. M. Davis, 1980: *Solar Radiation and Clouds.* Meteorological Monographs, vol. 17, no. 39. American Meteorological Society.

Welch, R. M., and B. A. Wielicki, 1985: A Radiative Parameterization of Stratocumulus Cloud Fields. *J. Atmos. Sci.*, 42, 2888-2897.

Wielicki, B. A., and L. Parker, 1994: Frequency distributions of cloud liquid water path in oceanic boundary layer cloud as a function of regional cloud fraction. 8th Conference on Atmospheric Radiation Preprints. American Meteorological Society, 415-417.